1.0 INTRODUCTION

The work carried out over the past 3 1/2 years under NREL Subcontract XAN-4-13318-07 has contributed toward the goals of two of the Amorphous Silicon Sub-Teams: toward understanding and improving the properties of the low-gap a-Si,Ge:H alloys, and toward developing more stable mid-gap a-Si:H materials. Much of our efforts have concentrated on the evaluation of materials produced by novel deposition conditions and/or methods. Specifically, in our low-gap related studies we have attempted to uncover the detailed electronic properties of deep defects in device quality a-Si,Ge:H produced by glow discharge at United Solar Systems Corporation, to compare the basic properties of this material with cathodic glow discharge alloy material produced at Harvard University, and to study the electronic properties of the a-Si,Ge:H/a-Si:H heterojunction interface. For our mid-gap materials related studies we carried out a detailed characterization of a series of hot-wire a-Si:H samples with varying hydrogen content deposited at NREL, of hydrogen diluted a-Si:H from three different laboratories, and of a-Si:H produced by an electron-cyclotron resonance enhanced deposition process at Iowa State University.

Our experimental results are based on a variety of techniques sensitive to the properties of defect states in semiconductors: admittance spectroscopy, drive-level capacitance profiling, and transient photo-capacitance (and photocurrent) spectroscopy. These characterization methods were used to determine electronic quantities important to the device performance of these amorphous semiconducting materials: the deep defect energy distributions and densities, Urbach bandtail energies, and the $\mu\tau$ products for holes. In most cases we examined the changes in the deduced electronic properties caused by light induced degradation. In several instances we also tried to compare the defect properties with transport property measurements and, for several series of samples, did find a clear relationship between the minority carrier processes and the deep defect density. One key finding from our studies in the low-gap alloy studies has been that the a-Si,Ge:H alloys at moderate Ge content deposited at Uni-Solar contain significant densities of charged deep defects. This results was based upon the identification of two distinct optical transitions in these materials and correlating the changes in their magnitudes with trace amounts of n- and p-type doping.

In the Sections that follow, we first describe the samples studied and review the experimental techniques employed. In Sections 4, 5, and 6 we present our detailed results involving the electronic properties of the a-Si,Ge:H alloy samples, and the a-Si,Ge:H/a-Si:H heterojunctions. In Sections 7,8, and 9 we present our results on the novel mid-gap materials: hot-wire, hydrogen diluted, and ECR deposited amorphous silicon, respectively. Finally, in Section 10 we summarize our findings and draw some general detailed conclusions.

2.0 SAMPLES AND SAMPLE TREATMENT

2.1 GLOW DISCHARGE AMORPHOUS SILICON-GERMANIUM ALLOYS

Nine a-Si,Ge:H films were deposited by the rf glow discharge method at United Solar Systems Corporation (courtesy of J. Yang and S. Guha). These were deposited on heavily p-type doped crystalline Si substrates at 300°C using mixtures of Si_2H_6 and GeH_4 gases diluted in H_2. The GeH_4 flow rate was varied to obtain different Ge fractions. Additional details of the deposition conditions have been described elsewhere [1]. The Ge fractions were determined by electron microprobe measurements, courtesy of Harv Mahan and Alice Mason at NREL. Seven of the samples studied had Ge fractions in the range 30 to 35at.%, considered the most suitable for the low gap alloy of tandem and triple solar cells. Five of these samples were undoped, one was n-type doped at a level of 2Vppm PH_3, and one was p-type doped at a level of 6Vppm BF_3. The remaining two samples were undoped and had Ge fractions near 20at.% and 50at.%, respectively. These samples were included to help identify behavioral trends in the alloy series.

To investigate the defect properties by our junction capacitance and photocurrent methods described below, semitransparent Pd contacts were evaporated on each film. However, in all the studies reported for these samples (see Section 4), the contact at the silicon substrate was employed as the active junction. The a-Si,Ge:H alloy samples were annealed at 460K for one hour before the initial series of measurements (state A). To study the light soaked states these samples were exposed for 70 to 100 hours to a focused tungsten halogen light source using an appropriate long pass filter to achieve uniform carrier generation rates over the 1 to 2μm thickness of each sample. Measured intensities for light soaking were 6W/cm^2 for the 30-35at.% alloys, 4.5W/cm^2 for the 50at.% alloy, and 6W/cm^2 for the 20at.% alloy. To maintain a low temperature during light exposure each sample was immersed in methanol. This guaranteed a surface temperature below 65°C.

2.2 CATHODIC AMORPHOUS SILICON-GERMANIUM ALLOYS

The a-Si,Ge:H samples were deposited by Paul Wickboldt of William Paul's group at Harvard University by the glow discharge method. However, unlike the deposition process used by most other groups, the substrates are attached to the rf electrode, which sustains a negative dc bias during deposition (the cathode).[2] In this method the mixtures of SiH_4 and GeH_4 gases were diluted in H_2. The flow rates of GeH_4 and H_2 were 1.00 sccm and 40.0 sccm, respectively. The SiH_4 flow rate was varied to obtain the different Ge fractions. The temperature of the substrates was kept constant at 225°C, the chamber pressure was maintained at 0.95 Torr, and the rf power density was 1.2 watts/cm^2 for all depositions. The films were grown on both heavily p^+ doped (111) oriented crystalline silicon wafers and on Corning 7059 glass.

TABLE I: Optical and electrical properties of the first series of cathode deposited glow discharge a-$Si_{1-x}Ge_x$:H alloy samples.

Sample No.	SiH_4 flow (sccm)	Ge content	Bandgap (eV) E_{04}	Bandgap (eV) E_{03}	E_σ (eV)	Thickness (μm) Optical	Thickness (μm) C-T-ω
479	1.60	57.3 at.%	1.57	1.39	0.666	2.83	2.61
478	1.00	67.5 at.%	1.53	1.37	0.645	3.07	3.08
477	0.70	74.5 at.%	1.44	1.30	0.620	2.99	2.77
476	0.37	84.5 at.%	1.40	1.24	0.559	1.97	1.96
427	0.00	100 at.%	1.26	1.12	0.510	—	2.28

Two series of films were deposited. The first consisted of five samples for which the Ge content was varied by varying the SiH_4 flow rate. We present the general optical and electrical properties of these films deposited at different flow rates of SiH_4 in Table I. The germanium content of each film was well determined by the electron microprobe method with an error less than 1at.%. The optical gaps E_{04} and E_{03} were measured at Harvard by optical absorption measurements on the glass substrate samples. The dark *ac* conductivity activation energy, E_σ, which we identify with the Fermi energy position, ($E_\sigma \approx E_C - E_F$), was deduced from the C-T-ω measurements for Schottky diode samples (see Section 4).

Both the optical bandgap and the dark *ac* conductivity activation energy decrease monotonically with increasing Ge content. We also note that E_σ is always less than one-half of E_{04} (or even E_{03}) implying that these alloys are effectively slightly n-type with a Fermi level above mid-gap. The fact that the film thicknesses obtained from capacitance match those derived from the optical absorption measurements indicates the same growth rates for films deposited on the different substrates.

TABLE II. Impurity levels of the second series, air contaminated cathodic a-Si,Ge:H samples.

Sample Number	Air Admixture (ppm)	Relative Oxygen Level	Relative Nitrogen Level
523	0	1	1
525	2	0.9	1.5
524	10	1.6	7.0
526	75	8.6	72

The second series of cathodic glow discharge a-Si,Ge:H alloys consisted of four films, each with an identical Ge content near 67at.%, but varying degrees of air contamination introduced by a controlled leak. This led to a varying level of nitrogen and oxygen impurity levels which were characterized by SIMS. The impurity levels for these four films are listed in Table II. These samples were again deposited onto both conducting crystalline Si as well as glass substrates. The latter allowed the characterization by coplanar transport methods; specifically, conductivity, photoconductivity, and the SSPG method. These transport measurements were carried out at Harvard University and their results, along with the results of our defect characterization on these samples are presented in Section 5.

2.3 AMORPHOUS SILICON/AMORPHOUS SILICON-GERMANIUM HETERO-JUNCTION SAMPLES

To investigate the electronic properties of the heterojunction between a-Si:H and the a-Si,Ge:H alloys, eight samples were also prepared by J. Yang and S. Guha at United Solar Systems Corporation. The substrates were heavily p-type doped crystalline Si and the alloy Ge fraction was 30-35at.% for all samples. All samples consisted of a 1.2-1.5μm a-Si,Ge:H alloy layer together with a 3000-5000Å layer of a-Si:H. For six samples the a-Si:H was deposited first, followed by the a-Si,Ge:H; however, for two samples this order was reversed. In two samples the transition between a-Si:H and a-Si,Ge:H alloy was graded rather than abrupt. And, in one case, the a-Si:H layer was subjected to a special surface treatment before the beginning of a-Si,Ge:H deposition. Table III provides the details of the configurations of the eight samples in this part of our study.

TABLE III. Summary of configurations for a-Si:H/a-Si,Ge:H heterojunction samples. The interface treatment for Sample 6 is a proprietary process of United Solar Systems.

#	First Layer	Interface	Second layer
1	a-Si:H (3000 Å)	Untreated	a-Si,Ge:H (1.2 μm)
2	a-Si,Ge:H (1.2 μm)	Untreated	a-Si:H (3000 Å)
3	a-Si:H (5000 Å)	Untreated	a-Si,Ge:H (1.2 μm)
4	a-Si,Ge:H (1.2 μm)	Untreated	a-Si:H (5000 Å)
5	a-Si:H (4000 Å)	Untreated	a-Si,Ge:H (1.5 μm)
6	a-Si:H (4000 Å)	Treated	a-Si,Ge:H (1.5 μm)
7	a-Si:H (4000 Å)	Graded (250 Å)	a-Si,Ge:H (1.5 μm)
8	a-Si:H (4000 Å)	Graded (1000 Å)	a-Si,Ge:H (1.5 μm)

Semitransparent Cr or Pd contacts (area of 2×10^{-3} cm^2) were evaporated on the top layer of each of these samples to form a Schottky barrier. Thus, the a-Si:H/a-Si,Ge:H interface was

positioned within 3000-5000Å of either this Schottky barrier of the substrate junction. This enabled its electronic properties to be probed capacitively. Results of our studies of these samples are presented in Section 6.

2.4 HOT-WIRE AMORPHOUS SILICON

A set of five a-Si:H films were deposited by Brent Nelson and Eugene Iwaniczko at NREL on stainless steel using the hot-wire CVD deposition technique. These films were also co-deposited onto p^+ crystalline Si substrates. However, except in a couple cases, these peeled off due to the larger inherent strain in these samples. By varying the substrate temperatures during deposition the hydrogen concentration in the films could be varied between more than 10at.% to less than 1at.%.[3] The deposition conditions for the film series is given in Table IV along with their hydrogen concentrations and thicknesses. The hydrogen concentrations were not actually measured for these samples, but are estimated on the basis of previous film depositions at the same temperatures.

We deposited semi-transparent Pd Schottky barrier on top of these films for our junction capacitance based measurements. Samples were examined in most cases both in a dark annealed "state A" and a light soaked "state B" achieved by illuminating the samples to a focused tungsten halogen light source (at an intensity of $5W/cm^2$) for 120 hours.

TABLE IV. Characteristics of hot-wire deposited a-Si:H samples.

Sample No.	Substrate Temp. (^oC)	Hydrogen Content (at.%)	Thickness (μm)
HW290	290	10-12	1.45
HW325	325	7-9	1.83
HW348	348	4-6	1.66
HW360	360	2-3	2.38
HW400	400	< 1	1.69

2.5 HYDROGEN DILUTED GLOW DISCHARGE AMORPHOUS SILICON

During this funding period we also examined three sources of a-Si:H material grown under hydrogen dilution. Such material has been determined to exhibit considerably less degradation when incorporated as the i-layer in photovoltaic devices. First, two glow discharge samples were obtained from Rajeewa Arya at Solarex. One was grown under their usual conditions for device quality material (pure silane discharge at a roughly 260^{o}C substrate

temperature), and the other was grown under conditions of hydrogen dilution (10:1 H_2:SiH_4 at somewhat lower substrate temperatures).

Second, we obtained a more extensive series of diluted and undiluted samples from collaborators at Lawrence Berkeley Laboratory (from the group of V. Perez-Mendez). They employed a conventional plasma enhanced CVD reactor employing an rf frequency of 85MHz. One sample was of their standard glow discharge sample material grown with 100% SiH_4, three samples were grown using mixtures of H_2 and SiH_4 in a ratio of 15-to-1, and two were grown using mixtures of He and SiH_4 in a ratio of 2-to-3. These six films were deposited on substrates of Corning 7059 glass and consisted of a n^+, intrinsic, and p^+ doped layers. The i-layers were at least 2μm thick. Substrate temperatures were varied between 190°C to 250°C. The top and bottom layers were contacted with sputtered semitransparent Cr. Details of the growth conditions for each of these samples are given in Table V.

In addition to these n-i-p samples, two additional sample configurations were studied. In one case, before deposition of the top Cr contact, the p^+ a-Si:H layer was removed using a SF_6 plasma etch, and then a Pd Schottky contact was deposited directly onto the exposed i-layer. This configuration will be referred to as an n-i-m structure. Also, a purely intrinsic a-Si:H layer was deposited directly onto a p^+ crystalline Si substrate, followed by the deposition of a Pd Schottky top contact. This will be denoted as the p^+(c-Si)-i-m sample.

TABLE V. Deposition conditions for the i layers of a-Si:H samples produced at Lawrence Berkeley Laboratory (courtesy of F. Zhong, W.S. Hong, and V. Perez-Mendez).

Sample (Dilutant)	$[H_2]/[SiH_4]$ $[He]/[SiH_4]$	Temperature (°C)	Pressure (mTorr)	Power Density (mW/cm^2)	Dep. Rate (μm/hr)	i-layer thickness
1 (H_2)	15	190	1000	60	1.4	5.2 μm
2 (H_2)	15	190	1000	90	1.5	6.2 μm
3 (H_2)	15	250	1000	60	1.1	4.8 μm
4 (He)	0.67	150	500	90	3.5-4	4.0 μm
5 (He)	0.67	250	500	90	3.5-4	7.8 μm
6 (none)	0.00	1.0	300	40	2.3	10. μm

Third, in a preliminary attempt to gain some insight into the mechanisms for improved stability in the hydrogen diluted material, we also carried out a feasibility study on three samples grown in our own glow discharge reactor. We grew one from a gas mixture of 30% SiH_4 diluted in hydrogen, a second sample using 30% SiH_4 diluted in argon, and a third sample in which SiH_4

again accounted for 30% of the mixture, but the dilutant gas was switched from H_2 to Ar every 10 to 15 minutes with a total of 34 layers. This resulted in a 4μm thick sample with a modulation period of about 2300Å. All substrates were heavily p-type crystalline Si and the substrate temperature was 200°C in all cases.

Defect densities in these samples were determined before and, in a couple cases, after light soaking using drive-level capacitance profiling. Light soaking was carried out using a red filtered tungsten halogen light source at a power level of 3.4W/cm^2. Samples were immersed in methanol during light exposure to ensure a low surface temperature (significantly below 65°C). The experimental results concerning the stability of these samples with respect to light-induced deep defect creation are presented in Section 8 below.

2.6 ELECTRON CYCLOTRON RESONANCE DEPOSITED AMORPHOUS SILICON

In addition to the hot-wire deposited and hydrogen diluted forms of a-Si:H, another new, potentially more stable form of a-Si:H is being developed as part of the amorphous silicon Mid-gap Team effort. This form of a-Si:H is produced by an electron cyclotron resonance (ECR) growth method at Iowa State University (under the direction of Professor Vikram Dalal). We thus obtained a series of several a-Si:H samples deposited onto stainless steel substrates. All of these samples incorporated an n+ a-Si:H layer at the substrate contact and each i-layer was roughly 1.5μm thick. A palladium Schottky contact at the top surface allowed us to probe their problems via our junction capacitance techniques. Included in this report are the results for 3 such samples: two grown under hydrogen dilution and one grown under helium dilution. Both the annealed and light soaked states were characterized by our methods and the results are reported in Section 9.

3.0 EXPERIMENTAL CHARACTERIZATION METHODS

The measurements employed in our studies rely on a set of experimental techniques which have all been described previously in some detail. For the purpose of this report we will describe each method briefly and review what kind of information is obtained from each type of measurement.

3.1 ADMITTANCE SPECTROSCOPY

Our Schottky diode samples contain a depletion region which is characterized as a function of temperature and frequency before we undertake the more sophisticated capacitance based measurements described in Sections 3.2 and 3.3 below. Such measurements provide us with an estimate of our film thickness (the temperature independent region at low T is simply related to the geometric thickness, d, by the formula $C = \varepsilon A/d$), and an Arrhenius plot of the frequency of the lowest temperature capacitance step (or conductance peak) *vs*. 1/T provides us with the activation energy of the ac conductivity, E_σ,[4] which we identify with the Fermi energy position: $E_\sigma \approx E_C - E_F$. These admittance measurements also give us an indication of the quality of our junction barriers which allow us to pre-screen our samples for further study.

3.2 DRIVE-LEVEL CAPACITANCE PROFILING

The drive-level capacitance profiling method has been described in detail in many publications [5,6]. It is similar to other kinds of capacitance profiling in that it provides us with a density vs. distance profile; however, this particular method was developed specifically to address the difficulties encountered in interpreting capacitance measurements in amorphous semiconductors. In this method we monitor the junction capacitance both as a function of DC bias, V_B, and as a function of the amplitude of the alternating exciting voltage, dV. One finds that to lowest order this dependence obeys an equation of the form:

$$C(V_B, dV) = C_o(V_B) + C_1(V_B)\, dV + \ldots$$

and that the ratio

$$N_{DL} \equiv \frac{C_o^3}{2q_e\, \varepsilon A^2\, C_1} \qquad (1)$$

is directly related to an integral over the density of mobility gap defect states:

$$N_{DL} = \int_{E_C - E_e}^{E_F^0} g(E)\, dE \qquad (2)$$

Here E_F^o is the bulk Fermi level position in the sample and E_e depends on the frequency and temperature of measurement:

$$E_e(\omega,T) = k_B T \log(\nu/\omega) \quad (3)$$

Thus, by altering the measurement temperature (or frequency) we obtain information about the energy distribution of the defects and, by altering the applied DC bias, we can vary the spatial region at which we detect the defects in the sample. That is, we can spatially profile the defects as a function of the position from the barrier interface.

Typically we employ 100Hz profiles for a series of temperatures between 320K to 380K. In Fig. 1 we show an example of such a series of measurements for a Uni-Solar a-Si,Ge:H sample up to a measurement temperature of 400K. In Fig. 2 we plot the spatially average values of N_{DL} obtained for this sample in both States A and B, as well as for two other a-Si,Ge:H samples, vs. the value of E_e obtained from the measurement temperature using Eq. (3). This figure shows that a clear upper limit for N_{DL} is obtained which we associate with the total defect density in each case (for a-Si:H, however, we believe this upper limit is reached after uncovering only a fraction of the defect band and thus usually multiply this value by a factor of 2). The maximum value of N_{DL}, which will also sometimes be denoted as TH1 in the Sections below, usually provides us with our best quantitative measurement of the deep defect density. In addition, we are able to assess the spatial uniformity of the electronic properties in these samples (see Fig. 1).

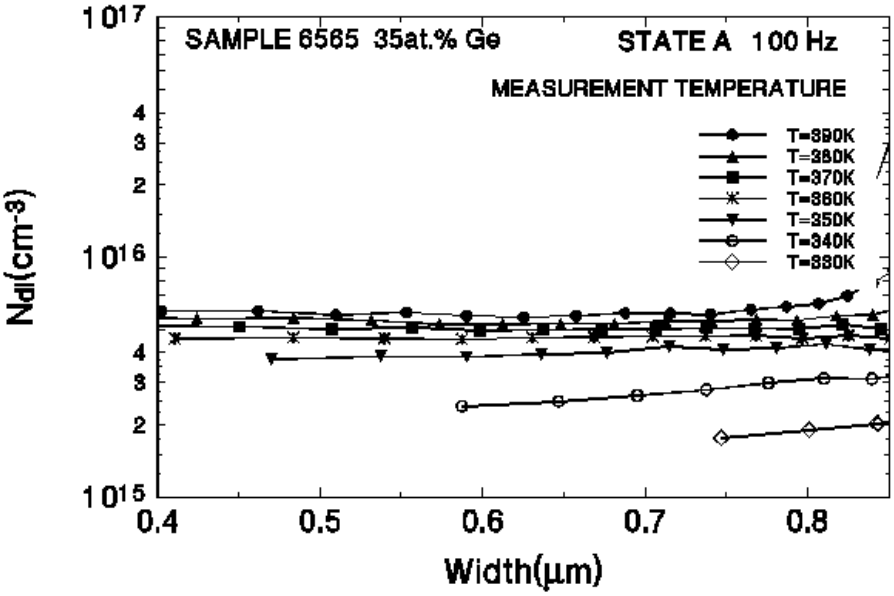

FIG. 1. Drive-level capacitance profiles for an a-Si,Ge:H sample produced by the glow discharge method at Uni-Solar. The 100Hz measurements were made at the temperatures indicated. The value in the highest measurement temperature limit (in this case 6×10^{15} cm^{-3}) provides an estimate of the total midgap defect density.

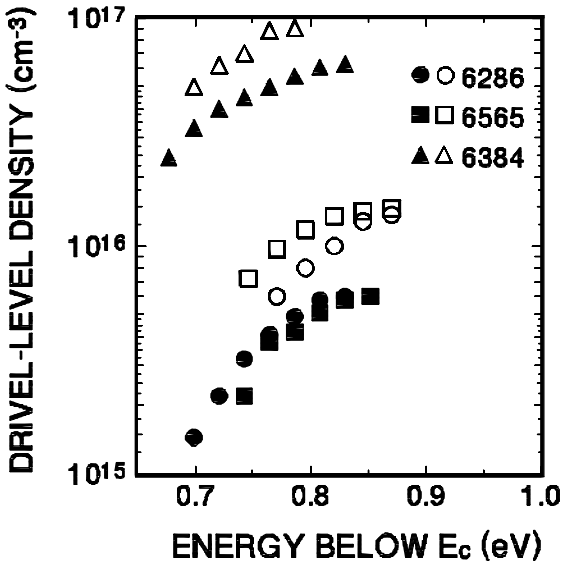

FIG. 2. Summary of drive-level densities vs. emission energy ($E_e = k_B T \log(\nu/\omega)$ for three a-Si,Ge:H samples: 6286 with 30at.% Ge, 6565 with 35at.%, and 6384 with 50at.% Ge. Closed symbols represent values for the annealed states of each sample, and open symbols the light soaked states. Note that all profiles reach a limiting value as E_e is increased.

3.3 TRANSIENT PHOTOCAPACITANCE AND PHOTOCURRENT

The general method of junction transient measurements on amorphous semiconductors has been discussed in detail in several earlier publications.[4,7,8] The basic physics of all such measurements is as shown in Fig. 4. We illustrate the situation for a semiconductor with one discrete deep gap states within the space charge region of a Schottky barrier which is subjected to a voltage "filling pulse". This pulse causes a non-equilibrium (filled) occupation of gap state to be established. As time progresses, the initial steady-state population is recovered through the excitation of trapped electrons to the conduction band where they can then move out of the depletion region under the influence of the electric field. In the dark this process proceeds entirely by the thermal excitation of trapped carriers. However, this process can be enhanced through optical excitation which is the basis of the photocapacitance and junction photocurrent techniques.

The re-equilibration can be observed by the redistribution of trapped carriers, either as a change in the *junction capacitance* (which occurs because the depletion region will contract as negative charge is lost and the positive charge density increases) or by monitoring the *current* which results from the motion of this charge. However, the capacitance transients have one significant difference compared to current transient measurements: The dominant type of emitted carrier (electron or hole) can be identified by the *sign* of the observed change in capacitance. Thus the direct comparison of capacitance and current transient measurements allows one to explicitly separate the electron and hole emission and/or transport processes.

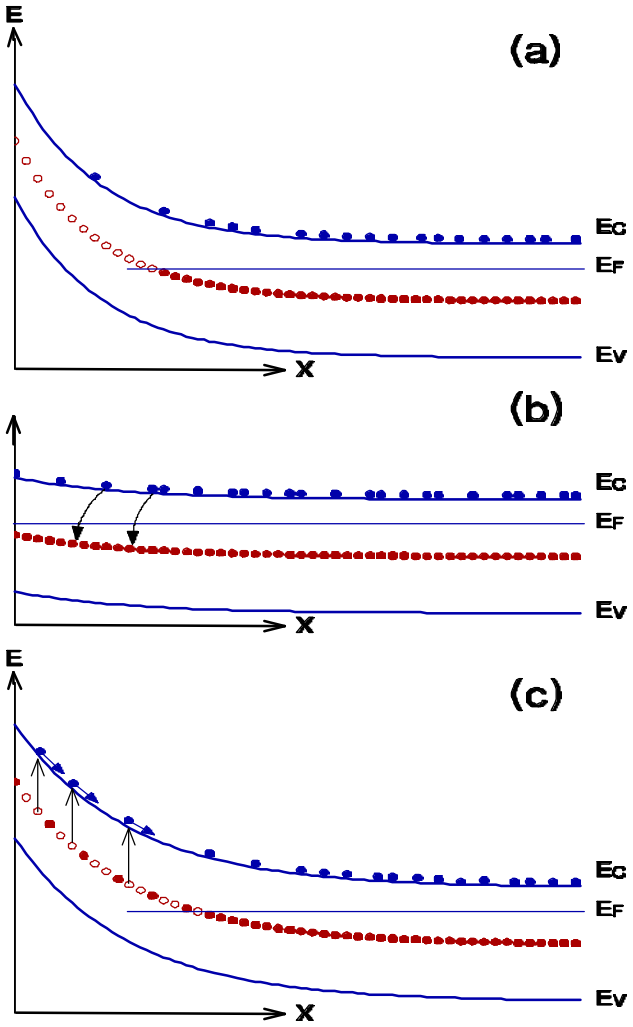

FIG. 3. Schematic diagram indicating the basic sequence of events in semiconducting junction transient measurements: **(a)** Junction under reverse bias in quasi-equilibrium showing the electronic occupation of gap states (solid circles) plus empty gap states above E_F in deep depletion (open circles). **(b)** During voltage "filling pulse" gap states capture electrons from the conduction band. **(c)** Reverse bias is restored and occupied gap states above E_F are slowly released to the conduction band due to thermal or optical excitation processes.

In our photocapacitance (or photocurrent) measurements we fix the temperature and record transients alternately in the dark and in the presence of sub-band-gap light. The experimental details to accomplish this have been discussed previously.[9,10,11] We then define the photocapacitance (or photocurrent) signal, $P(E_{opt})$, to be the photon flux (Φ) normalized difference in the integrated transient signals recorded with and without the presence of the sub-band-gap light of optical energy E_{opt}. The photocapacitance *spectrum* is obtained by plotting P *vs*. E_{opt} at constant T. We take special care to always operate in the low light intensity limit (where P is intensity independent). Thus the photocapacitance spectrum reveals the distribution of allowable transitions for an electronic population of gap states not appreciably disturbed by the optical excitation, but rather determined by the application of the voltage pulse followed by whatever thermal evolution takes place within the time before the transient is recorded.

Several examples of photocapacitance spectra are given in the following sections and have the general appearance of spectra obtained by the perhaps more familiar steady-state sub-band-gap optical techniques, such as photo-thermal deflection spectroscopy (PDS) [12] or the constant photocurrent method (CPM). [13] Indeed, one encounters a rather similar expression in

the interpretation of our transient photo-spectra in terms of a convolution between localized gap states and extended states connected by an optical matrix element for the transitions. Specifically, for transitions from gap state electrons to the conduction band one expects a contribution to P given by [10,11]:

$$P_n^C(E_{opt},T) = K_n(T) \int_{E_C-E_{opt}}^{E_C-E_e} \left|\langle i|ex|f\rangle\right|^2 g(E)\, g_C(E+E_{opt})dE \qquad (4)$$

where $|\langle i|ex|f\rangle|^2$ represents the optical matrix element, and $K_n(T)$ is a constant that depends on the temperature as well as the overall depletion width and the time window parameter τ (and also the frequency for the case of capacitance measurements). It will also depend on the ability of the carriers, once optically excited into the conduction band, to leave the depletion region. Thus K will depend on the electric field distribution within the depletion region and the electron mobility. However, all of these factors will be roughly constant (independent of optical energy) for a given temperature and applied bias. One should also note that the upper limit of the integral is determined by the thermal escape depth, E_e, of gap state electrons to the conduction band at the measurement temperature and time window, τ, as given by Eq. (3) with $1/\tau$ substituted for ω. That is, the optical transitions from these shallower electronic levels will be missing from the photocapacitance spectrum because they will have escaped thermally before the photocapacitance signal is recorded.

We should stress that the expression given in Eq. (4) represents only one contribution to the photocapacitance or photocurrent signals. A similar expression [giving a quantity we might label $P_p^V(E_{opt})$] must be included to take into account transitions from the valence band into empty gap states. The leading constant will then be replaced by $K_p(T)$ which contains information about how easily the optically excited holes will leave the depletion region.

There are actually two other sub-band-gap optical processes that must be considered as well. First of all, an electron from the valence band can be excited into an empty gap state that is close enough to E_C that it will subsequently thermalize into the conduction band. This will occur on the timescale of our measurement if it lies within an energy E_e of conduction band mobility edge, and can be represented by the integral

$$P_n^V(E_{opt},T) = K_n(T) \int_{E_C-E_e}^{E_C} \left|\langle i|ex|f\rangle\right|^2 g(E)\, g_V(E-E_{opt})dE \qquad (5)$$

With such a process there is also a hole left in the valence band. And, there will be an analogous integral expression for P_p^C resulting from optical transitions from deep in the mobility gap to the conduction band such that the hole that is left in the gap will thermalize the valence band on the measurement timescale.

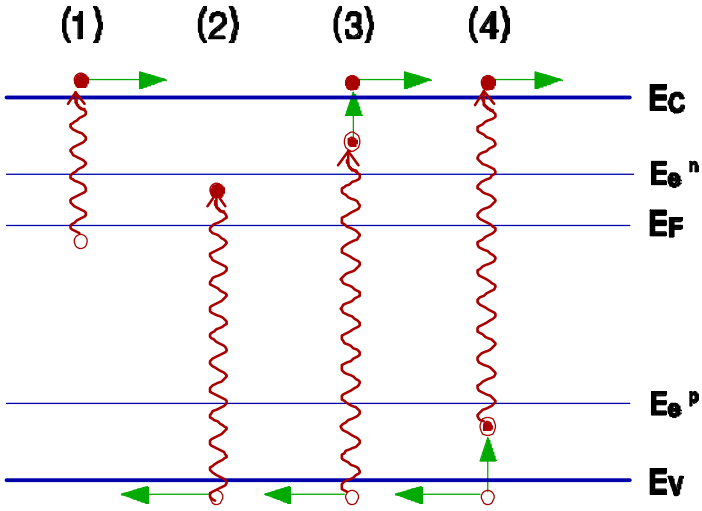

FIG. 4. Schematic diagram of the types of optically initiated deep defect transitions. As discussed in the text, these contribute differently to the photo-capacitance and the transient photocurrent signals. Here optical transitions are indicated by wavy lines and thermal transitions are indicated by solid vertical lines. Horizontal arrows indicate electron and hole transport out of the depletion region. The dashed horizontal lines for the hole motion illustrate the fact that holes are more likely to be re-trapped before escaping the depletion region.

A schematic diagram indicating these four types of processes in given in Fig. 4. Without additional information it is obvious that a single type of sub-band-gap spectrum will not allow one to distinguish the above possible contributions responsible for the observed signals. For example, PDS measurements are totally insensitive to the subsequent motion of carriers and therefore have absolutely no way to distinguish between such different types of transitions. Some proponents of the CPM method argue that at low temperatures one can generally neglect the contribution of minority carrier motion to the current signal. However, one still has no way to separate the contributions to the electron current from the types of processes labeled (3) and (4) in Fig. 4. Indeed, the contribution of processes of type (3) has often been completely neglected in the analysis of CPM spectra that have appeared in the literature.

Our studies, which compare the photocapacitance and photocurrent spectra resulting from the same set of electronic transitions, provide one of the few methods to identify the different types of transitions in Fig. 4 since these contribute differently for a photocapacitance as opposed to a photocurrent spectrum. Many examples of photocapacitance and photocurrent spectra are given in the next Section. We also discuss the procedure followed to analyze these spectra in terms of the types of transitions shown in Fig. 4.

4.0 ELECTRONIC PROPERTIES OF THE UNI-SOLAR a-Si,Ge:H ALLOYS

4.1 DEEP DEFECT PROPERTIES AND DEGRADATION

As described in Section 2, we examined nine a-Si,Ge:H alloy films deposited by the rf glow discharge method onto heavily p^+ doped crystalline silicon substrates at United Solar Systems Corporation.[1] Seven of these samples were close to intrinsic, although two samples, referred to as ν-type, were found to have Fermi levels 50 to 100meV shallower than the most intrinsic samples. The two remaining samples were intentionally doped with 2Vppm PH_3 and 6Vppm BF_3, and will be referred to as the n- and p-type samples, respectively.

All samples were annealed at 460K for one hour before the initial series of measurements (state A). To study the degraded state, samples were light soaked with an appropriate long pass filter to achieve uniform carrier generation rates. Light exposure on a-Si,Ge:H alloys was at 6W/cm^2 for 70 hours with the samples immersed in methanol to maintain a surface temperature below 65°C (state B).

As described in Section 3.2 above, the DLCP method provides our best quantitative estimate for the overall density of deep defects. Figure 5 presents the deep defect densities for 8 of our samples determined by this method (the p-type sample is omitted) for both states A and B. Except for the n-type sample we find defect densities at or slightly below 1×10^{16} cm^{-3} for all of the 35at.% Ge samples, and these increase by roughly a factor of 2 after light soaking. The n-type and the 50at.% Ge sample defect densities are closer to 10^{17} cm^{-3} and increase only by a factor of 1.3. These defect densities are lower than most others reported in the literature in this composition regime, and are roughly comparable to those of the photo-CVD a-Si,Ge:H alloy samples obtained from the University of Delaware we had reported a few years ago [14]. However, we note that the spatial uniformity of the Uni-Solar samples revealed by the DLCP measurements (see Fig. 1) are significantly better than for the photo-CVD samples.

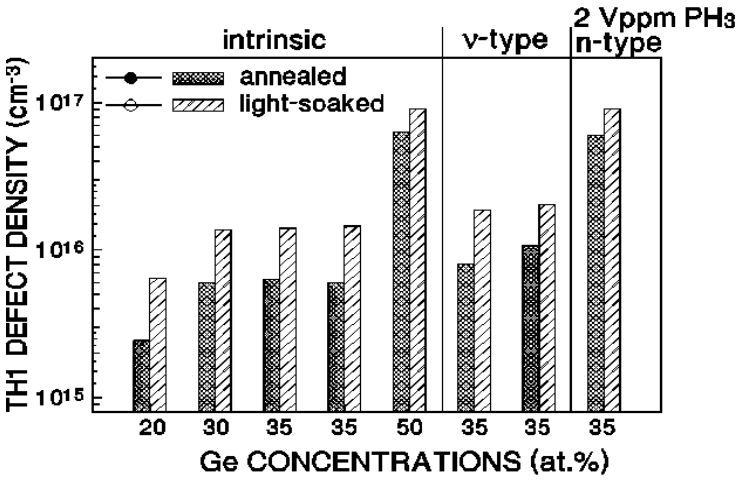

FIG. 5. Bar graph indicating the magnitudes of the DLCP determined TH1 band for 8 a-Si,Ge:H samples in the annealed (dark bars) and light soaked states (lighter bars). The Ge fractions are shown on the bottom scale, and the doping levels are indicated at the top of the figure.

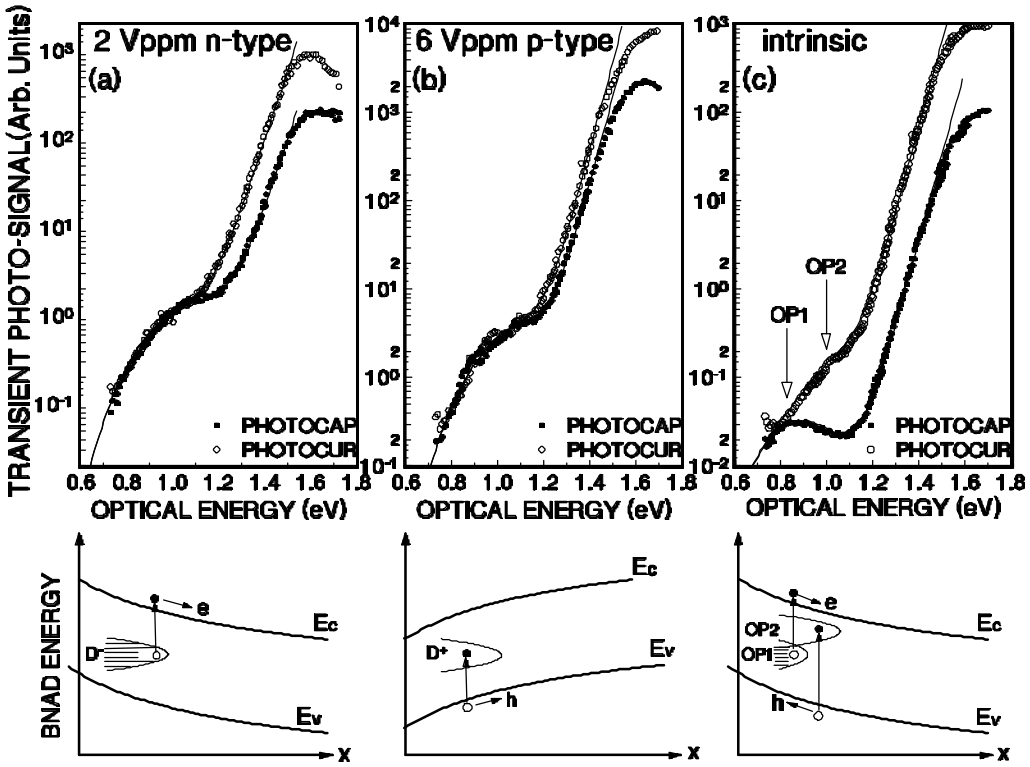

FIG. 6. Pairs of photocapacitance and photocurrent spectra for three a-Si,Ge:H samples containing 35at.% Ge. (a) n-type doped, (b) p-type doped, and (c) intrinsic. The thin lines through the data points are fits using the types of defect optical transitions indicated below each set of spectra. The densities of states used to fit these spectra are shown in more detail in Fig. 7.

Next, we recorded transient photocapacitance (TPC) and transient junction photocurrent (TPI) spectra for each of these samples at several temperatures in both the annealed and light soaked states. As described in Section 3.3 above, and in the literature [15,16,17], the TPC method records the residual charge change due to weak optical excitation within the depletion region on the measurement timescale (400ms in our case). Because transitions to the majority band increase the depletion capacitance, while transitions to the minority band decrease the depletion capacitance, the TPC spectra indicate the *difference* between these two types of transitions. On the other hand, the current due either to majority or minority carriers has the same sign so that the TPI spectra reveal the *sum* of the two types of transitions. Taken together, these two types of spectra indicate whether defect transitions involve the majority or minority carrier bands.

Figure 6(a) shows TPC and TPI spectra for the 2 Vppm n-type doped sample. A dc potential of 3 volts was applied to place the substrate p^+n junction into reverse bias. Here the spectra are fit using only a single defect sub-band with electronic excitations to the conduction band. This sub-band should correspond to D^- centers because these dominate at even moderate n-type doping levels. Because only an electron current results from the optical transitions of this defect sub-band, both the TPI and TPC spectra are seen to overlap perfectly outside of the band tail regime. On the other hand, within the band tail region, each optical transition results in one

conduction band electron plus one valence band hole. This leads to a distinct decrease in the TPC relative to the TPI spectrum due to the motion of the hole. The magnitude of this decrease actually depends on the relative carrier mobilities and has been used to estimate the hole $\mu\tau$ product in several previous studies.[17-20] Estimates of the hole $\mu\tau$ products for the present series of samples will be described in Section 4.2.

Figure 6(b) shows the optical spectra for the 6 Vppm p-type doped sample. Here we also find only a single defect sub-band of optical transitions is needed to fit the spectra. This now corresponds to D^+ defects. This sample incorporates a thin layer of n^+ a-Si:H on top of the film and the band bending in the major depletion region is at the top junction and is *downward*.[21] Therefore, it is now the majority *hole current* induced by the optical transition that is responsible for the TPI and TPC signals (this is confirmed by the *sign* of the TPC signal). The perfect overlap of these two spectra outside the band tail region verifies that there is only a single type of defect transition involved.

Figure 6(c) shows a typical spectra for a 35 at.% Ge intrinsic sample. Here things have obviously become more complex. Indeed, we now need *two* bands of defect transitions to fit the spectra. One corresponds to optical transitions which remove an electron from a defect sub-band into the conduction band, while the other corresponds to transitions which insert a valence band electron into an unoccupied defect sub-band. We have previously denoted these two bands of optical transitions as "OP1" and "OP2", respectively.[19,22] Like the case for the n-type film, the major depletion region for the intrinsic samples is at the substrate junction with an upward band bending. Also, because the Fermi level is slightly closer to the conduction band, the optically induced current *at threshold* will be totally due to electrons excited out of defect levels. Therefore, the TPC and TPI spectra should be strictly proportional at these lowest optical energies and so we overlap them in this region. While the optical transitions for the OP1 sub-band will continue to contribute equally to the TPC and TPI spectra, the hole current arising from OP2 sub-band of optical transitions will contribute oppositely to the TPC and TPI signals. This results in the large separation of the two spectra at intermediate optical energies.

The intrinsic sample spectra actually exhibit a separation that is larger near 1.1eV than in band tail region (above 1.3eV). As we have discussed previously [16,17,19,22], this implies that the valence band electrons inserted into the OP2 defect sub-band are not released for times longer than the measurement time window (0.4 sec). Thus we had hypothesized that the responsible defect sub-band for OP2 would more likely correspond to D^+ (rather than D^o) Ge dangling bonds since these would have a large thermal barrier for re-emission of the electrons being optically inserted from the valence band.

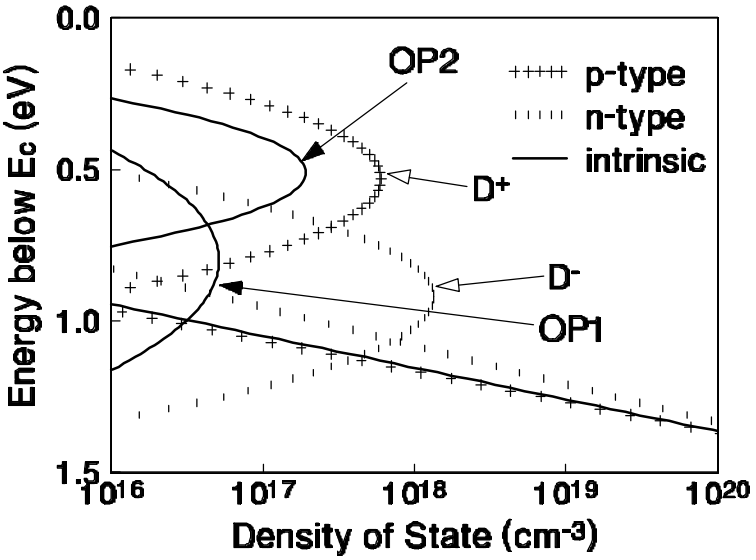

FIG. 7. Energy distributions of defect bands used to fit the three sample spectra of Fig. 6. Light induces transitions *out of* the bands labeled OP1 or D^- into the conduction band, and induces transitions from the valence band *into* the bands labeled OP2 or D^+. Note the good match between the D^+ band of the p-type sample and the OP2 band of the intrinsic sample.

The optical defect transition bands for the three samples of Fig. 6 are summarized in Fig. 7. We can see clearly that the OP2 sub-band is nearly identical in energy to the D^+ defect sub-band in the p-type sample and this confirms its identification with this sub-band. Therefore, these optical spectra clearly demonstrate that there are significant positively charged defects in intrinsic glow discharge a-Si,Ge:H alloys. Because of charge neutrality, there must also exist a similar density of negatively charged defect states in these intrinsic samples. However, the OP1 sub-band of the intrinsic samples has a different shape and energy position compared to the D^- defect sub-band in the n-type sample. Therefore, the OP1 sub-band is probably *not* a reliable indicator of the magnitude of the D^- defect sub-band (that is, it more likely involves transitions from a *superposition* of the D^- and D^o sub-bands).

Figure 8 displays the changes that occur to the TPC and TPI spectra upon light soaking for the intrinsic sample of Fig. 6(c). Although the spectra have a markedly different appearance

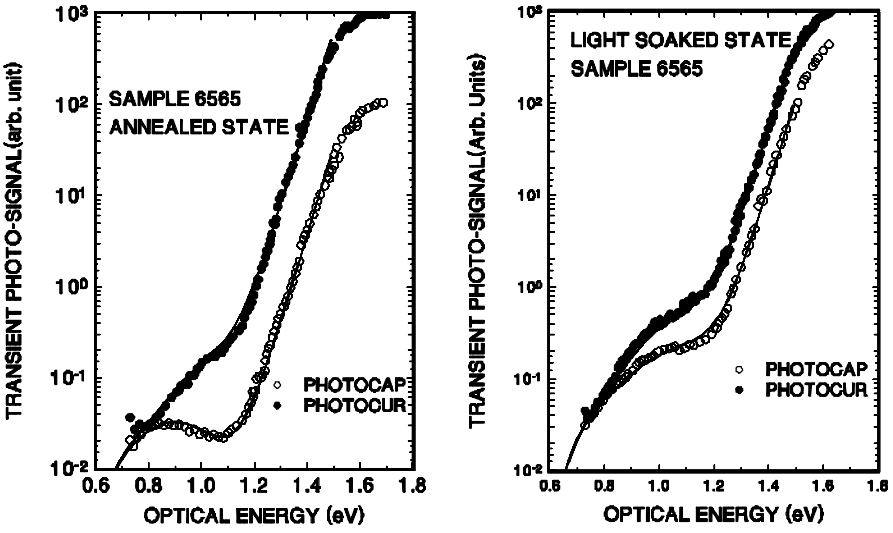

FIG. 8. The transient photocapacitance and photocurrent spectra for the annealed and light soaked state of the intrinsic 35at.% Ge sample of Fig. 6(c). The solid lines drawn through the data points represent the results of a model calculation incorporating two optical bands for the deep defect transitions: OP1 and OP2, as shown in Fig. 9.

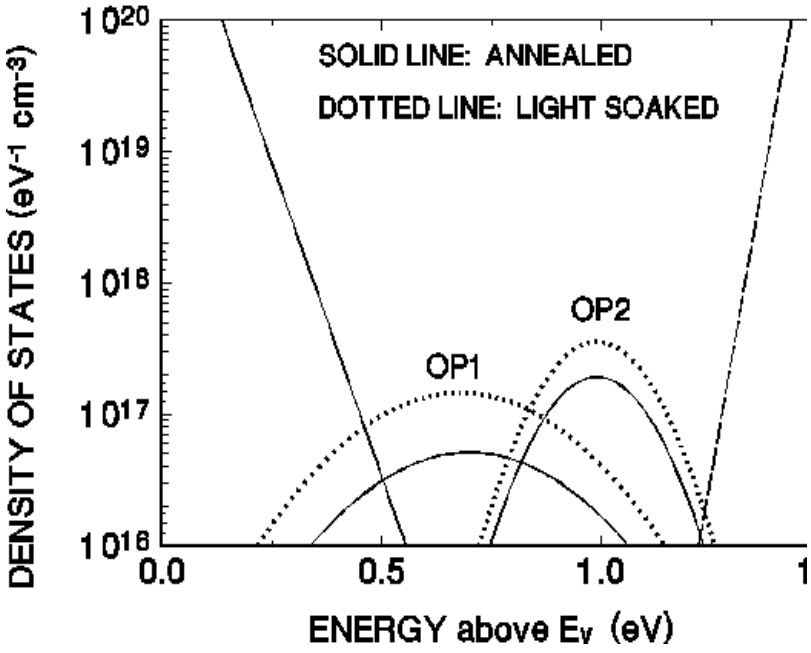

FIG. 9. Densities of states employed to fit sub-band-gap optical spectra of Fig. 8. Light induces transitions *out of* the band labeled OP1 into the conduction band, and induces transitions from the valence band *into* the band labeled OP2. The valence band-tail region is also incorporated into the fitting procedure and thus yields a value for the Urbach energy. The conduction band-tail distribution is not incorporated into the fits and is shown only for illustration.

compared to the state A spectra, most of this is caused by the lower hole mobility which results in a smaller separation between the two types of measurements (see Section 4.2). Indeed, the defect structure deduced from fitting the spectra after light soaking (Figure 9) is essentially unchanged except for the magnitudes of the deep defect transitions. The result of this fit shows that both bands of optical transitions, OP1 and OP2, increase by factors between about 2 and 3 after degradation. In Table VI we summarize the magnitudes for OP1 and OP2 deduced by fitting the TPC and TPI spectra in both states A and B for all of the a-Si,Ge:H samples in this study. (The defect densities obtained for TH1 deduced from the DLCP measurements have also been included.)

Although we have identified OP2 with the D^+ sub-band of defect states, we noted that OP1 did not seem to correspond to a particular defect sub-band. Indeed, in Fig. 10 we have plotted the ratios OP2/OP1 for the intrinsic and n-type samples before and after light soaking. These ratios indicate that there is no simple correlation between the magnitudes of these two sets of defect transitions. On the other hand, a clearer relation exists between OP2 and the magnitudes of the TH1 transition revealed by the DLCP method. The DLCP measurement detects the thermal emission of trapped charge to the majority carrier band so that, in intrinsic and n-type samples, the responsible deep defects must contain at least one electron. Moreover, because electrons bound to D^- defects are more easily thermally emitted, TH1 is more likely to be weighted toward the D^- defect density. Indeed, the defect densities plotted in Fig. 5 indicate that, for the 35at.% Ge samples, the TH1 density increases as the n-type doping level increases. From Table VI we also see that the OP2 density determined by the TPC and TPI methods exhibits a decreasing trend with increasing n-type doping, again consistent with our identification of OP2 with the D^+ defect sub-band.

TABLE VI. Defect sub-bands densities of a-Si,Ge:H alloys determined by C-T-ω, DLCP, junction transition photocapacitance and photocurrent methods before and after light soaking. The errors which come from the simulation for estimating OP1 and OP2 are about ±4at% and ±8at% respectively.

Sample (type)	Ge content	State	Ec-E_F (eV)	TH1 (10^{15}/cm^3)	OP1 (10^{16}/cm^3)	OP2 (10^{16}/cm^3)
6230	20 at.%	A	0.73	2.4±0.3	0.64	1.88
(intrinsic)		B	0.75	6.5±0.6	1.46	3.62
6286	30 at.%	A	0.70	6.0±0.3	1.99	5.18
(intrinsic)		B	0.75	13.7±0.9	6.63	7.54
6558	35 at.%	A	0.71	6.3±0.4	4.38	4.42
(intrinsic)		B	0.73	14.0±1.2	7.91	7.73
6565	35 at.%	A	0.75	6.0±0.3	2.56	4.82
(intrinsic)		B	0.75	14.5±1.2	7.32	8.93
8257	35 at.%	A	0.66	8.0±0.4	3.86	1.34
(ν-type)		B	0.75	18.6±0.9	4.15	3.93
8330	35 at.%	A	0.65	10.7±0.1	2.29	1.25
(ν-type)		B	0.69	20.4±1.3	4.07	4.05
8258	35 at.%	A	0.56	60.0±2.5	43.8	0.00
(n-type)		B	0.64	90.2±6.0	69.9	0.00
(p-type)	35 at.%	A	>0.80	—	0.0	21.0

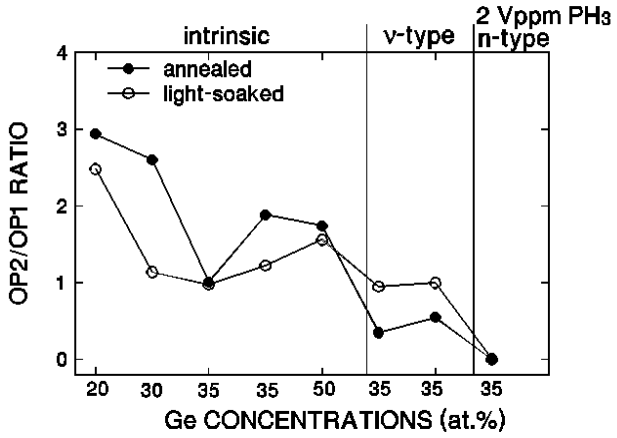

FIG. 10. Ratios of the magnitudes of the two defect bands, OP2/OP1, derived from analysis of the optical spectra. Note the fairly substantial variation of this ratio depending on the sample and metastable state. This argues against a simple identification of the OP1 band in terms of a specific defect sub-band.

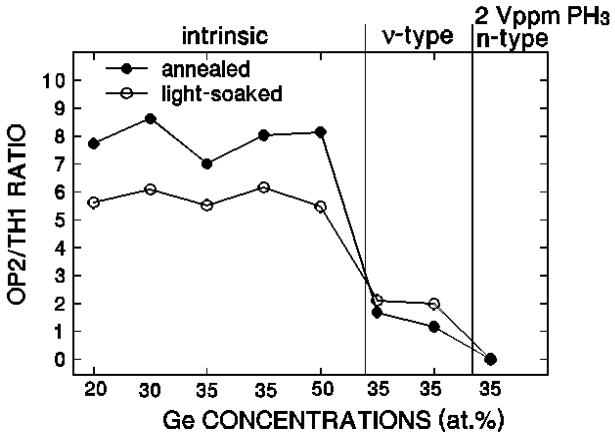

FIG. 11. Ratios of the magnitude of the OP2 (D^+) band to TH1, the DLCP determined defect density. The nearly constant ratio for the intrinsic samples, and the decreasing ratio for the ν- and n-type samples, strongly suggests that TH1 is closely associated with the D^- sub-band.

In Fig. 11 we plot the *ratio* of OP2/TH1 for all the samples and see that it is nearly identical for all intrinsic samples in the annealed state and also in the light soaked states. This correlation between the TH1 and the OP2 defect sub-bands strongly suggests that the TH1 defect

sub-band indeed corresponds to D^- centers by charge neutrality. Also, we see that the OP2/TH1 ratios become smaller for the ν-type samples as would indeed be expected for the D^+/D^- ratios. Finally, the D^+/D^- ratios should increase in the ν-type samples after light soaking and this is also indicated. All of these results strengthen our argument that TH1 defect sub-band corresponds closely to D^- centers while OP2 corresponds to D^+ centers. Also, since the DLCP measurements provides an absolute value for the defect density while the optical measurements depend on estimates of optical cross-sections, this identification provides a better calibration of the actual defect densities in these samples That is, the densities listed for OP2 should probably be divided by roughly a factor of 6 to 8 to match the values of TH1 in the most intrinsic samples.

Thus we believe we have obtained quite strong experimental evidence for the existence of significant densities of charged defects in device quality a-Si,Ge:H alloys. This realization must significantly alter any future analyses of a-Si,Ge:H based photovoltaic devices. However, because our methods do not provide a clear signature for the density of neutral defects, we do not yet have a good estimate for the ratio of charged to neutral defects. Experiments to compare ESR measurements with the results of the above types of studies are planned for the near future to pin down this ratio.

Finally, we note that when these types of measurement methods were previously applied to amorphous silicon samples (a-Si:H), they did *not* yield any such evidence for charged defects.[15,17] Moreover, comparison studies between ESR and capacitance studies in a-Si:H have indicated fairly consistent agreement between densities of deep defects.[23] This tends to suggest a predominance of *neutral* defects in intrinsic a-Si:H. Thus there appears to be a fundamental difference between a-Si:H and the a-Si,Ge:H alloys. This may be due to the lower correlation energy for Ge vs. Si dangling bonds, or to larger potential fluctuations in the alloys.

4.2 RELATION BETWEEN MINORITY CARRIER TRANSPORT AND DEEP DEFECTS

In this Section we shall examine the relationship between the hole transport characteristics, obtained using two different experimental methods, and the deep defect densities obtained from the measurements described above. In addition to the deep defect densities there are two other pieces of information that can be obtained from the sub-band-gap photocapacitance and photocurrent spectra. First, one obtains the bandtail slope or Urbach energy. This is an important quantity which may indeed affect the effective hole mobilities. However, for the current series of samples, the Urbach energies are nearly equal. Therefore, this is not a quantity which could account for any significant differences in minority carrier transport.

Second, the ratio between the bandtail signal for the photocapacitance and photocurrent signals provides a measure of the escape probability of the optically induced free holes from the depletion region. This is because the hole currents *add* to any electron currents caused by the

optically induced release of trapped carriers, but *subtract* from the resultant charge changes in the depletion region, as monitored by the photocapacitance technique. Thus the ratio between the two is directly related to the hole $\mu\tau$ products. Because of the long time scales of this measurement method the τ obtained is specifically a deep trapping time.

As discussed in Section 4.1 above, we align the two types of spectra at the lowest optical energies. This makes sense referring back to Fig. 4 since, at the lowest optical energies, we expect only to be able to excite a single carrier type [transition (1) in Fig. 4]. Thus the two types of spectra can be calibrated by matching them to each other in this energy regime. Referring to the spectra in Fig. 6, we then observe that the ratio of the photocapacitance and photocurrent signals in the bandtail region (optical energies greater than about 1.2 eV) differ only by a constant factor. This happens because optical excitation near the optical gap leads to the generation of free electrons and holes in roughly equal numbers. [See transitions (3) and (4) in Fig. 4] If both types of carriers were to escape the depletion region with equal probability, the net charge change, and hence the transient photocapacitance signal, would be nearly zero. However, the transient photocurrent signal would be enhanced. In general, then, the degree of suppression of hole escape will decrease the relative ratio, R, of the photocapacitance to the photocurrent signals, and this ratio can be used to determine the retrapping distance of the liberated hole, and hence $(\mu\tau)_h$.

As presented in detail elsewhere [14,15,16], we have derived an explicit expression for $(\mu\tau)_h$ in terms of R and the charge density, N_+, in deep depletion of our sample. This latter quantity is obtained experimentally by our drive-level profiling measurements in the limit of increasing temperature (that is, it is equal to the magnitude of TH1). We obtain [24]

$$(\mu\tau)_h = \frac{\varepsilon}{q_e N_+} \log [(R + 1)/2R] \qquad (6)$$

We can illustrate the use of this formula for the data exhibited in Fig. 6(c). The ratio for optical energies above $h\nu = 1.3$eV is roughly constant at $R = 0.05$, and our drive level measurements give $N_+ = 6 \times 10^{15}$ cm^{-3}. Hence we obtain $(\mu\tau)_h = 2 \times 10^{-9}$ cm^2/V. Note that the value we obtain depends on the measurement temperature but reaches a limiting value as temperature is increased. It is this limiting value that we report. Indeed, our $(\mu\tau)_h$ evaluation is quite consistent with trapping time derived $(\mu\tau)_h$ products determined by other methods [25].

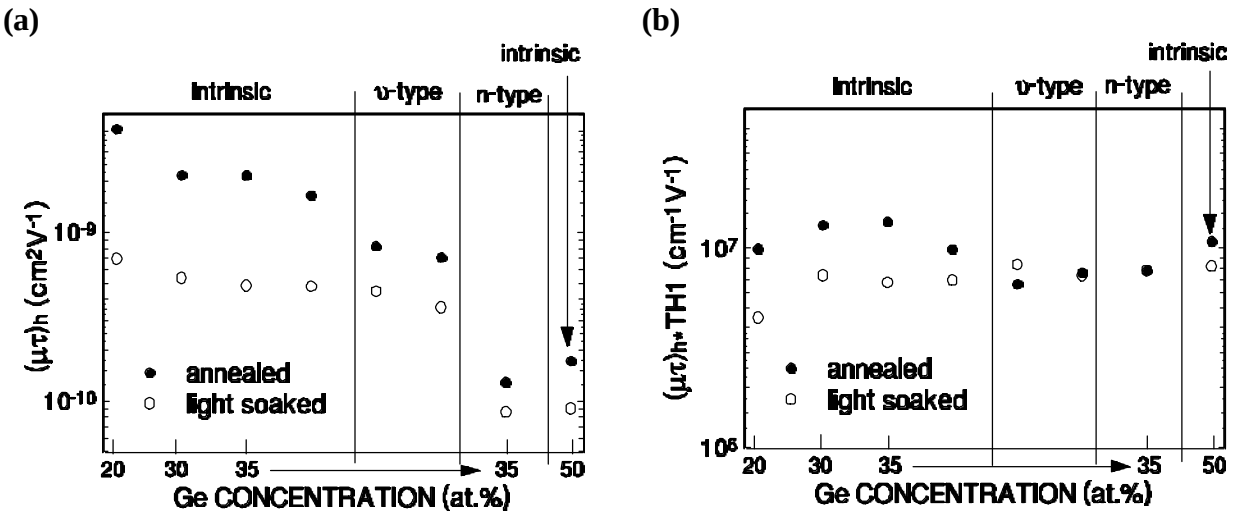

FIG. 12. (a) Dependence of the hole μτ products deduced from the analysis of the photocapacitance/photocurrent ratios on alloy composition. (b) The variation of $(\mu\tau)_h$ multiplied by the corresponding negatively charged defect densities [that is, $(\mu\tau)_h$ TH1]. Note the nearly constant value, independent of alloy composition, doping, or metastable state.

In a like manner we have determined $(\mu\tau)_h$ for most of our other a-Si,Ge:H samples. The dependence of this quantity on Ge content, x, is displayed in Fig. 12(a). [20] We clearly observe a monotonic *decrease* in $(\mu\tau)_h$ as the n-type doping or the Ge fraction is increased. It is also dramatically decreased following light induced degradation. Since the density of defects *increases* under the same conditions, the observed decrease in $(\mu\tau)_h$ may simply reflect the increased likelihood of deep trapping due to the extra defects. Moreover, it is more likely that the holes will be trapped in the negatively charged defects which, we have argued above, are most closely correlated with TH1. Thus in Fig. 12(b) we plot the product $(\mu\tau)_h$TH1. Indeed, we then observe a nearly constant dependence independent of Ge content, doping, or metastable state. This is particularly true for the highest defect samples. The observed deviations for the lower defect samples suggests there are other factors that also influence the hole μτ products in those cases.

To further test the relationship between minority carrier transport and defect density, we also examined two additional Uni-Solar samples of different Ge fractions, 0.20 and 0.35, that were deposited simultaneously on conducting and insulating substrates. The conducting substrate samples were used for defect density measurements based on our junction capacitance measurements. Specifically, sub-band-gap (photocapacitance) measurements were carried out to determine the Urbach energies and to provide one estimate of the deep defect density. The DLCP measurements provided a second measurement of the deep defect density. For the films on the insulating substrates, dark and photoconductivity as well as SSPG measurements were

TABLE VII. Properties of two a-Si,Ge:H alloy samples grown at Uni-Solar in both their annealed (state A) and degraded conditions (state B). The deep defect density is that determined by drive-level capacitance profiling measurements. The values for $\eta\mu\tau$ and ambipolar diffusion lengths were obtained from photoconductivity and SSPG measurements, respectively.

Ge fraction (at.%)	STATE	E_σ (eV)	Urbach slope (meV)	TH1 defect density (cm^{-3})	OP1 defect density (cm^{-3})	$\eta\mu\tau$ ($cm^2\ V^{-1}$)	L_{amb} (Å)
20	A	0.8	48	5×10^{16}	1.3×10^{16}	1.6×10^{-6}	650
20	B	0.75	48	1.8×10^{16}	2.75×10^{16}	2.4×10^{-7}	550
35	A	0.63	51	1.9×10^{16}	6.6×10^{16}	7.1×10^{-7}	540
35	B	0.70	51	3.05×10^{16}	8.2×10^{16}	6.6×10^{-8}	460

carried out to determine values the activation energy of dark conductivity, E_σ, the mobility-lifetime products, $\eta\mu\tau$, and the ambipolar diffusion lengths, L_{amb}. All of the above quantities were determined in a dark annealed state (state A) as well as the light-soaked state (state B). The results are given in Table VII. In addition, the values obtained for the ambipolar diffusion length and the deep defect density obtained from the DLCP measurements are displayed graphically in Fig. 13.

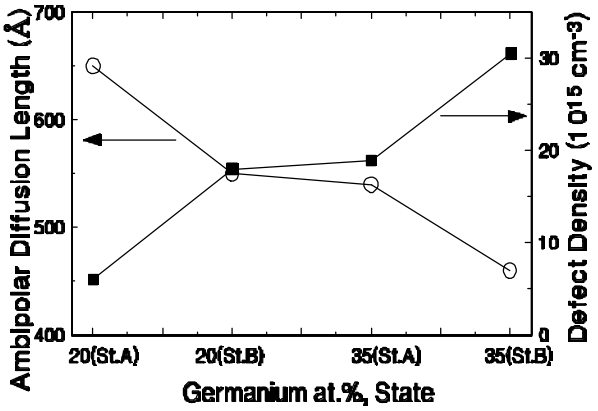

FIG. 13. Variation of the SSPG determined ambipolar diffusion lengths for two Uni-Solar a-Si,Ge:H samples in States A and B (left-hand scale) together with the corresponding defect densities determined by DLCP (left-hand scale).

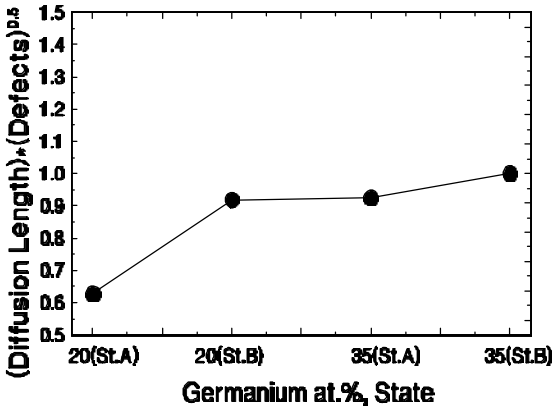

FIG. 14. Product of the ambipolar diffusion length and the square root of the deep defect density. If the diffusion length is controlled by that defect density, then this product should be nearly constant.

If, as suggested above, the quantity limiting the hole transport is the negatively charged deep defect density, then L_{amb} should be proportional to the inverse of the *square root* of the DLCP determined defect density, TH1. The implies that the quantity $L_{amb} \times TH1^{1/2}$ should be nearly constant. This quantity is plotted in Fig. 14.

The nearly constant value for the higher defect density cases confirms that the TH1 determined (negatively charged) defect density is indeed the dominant factor limiting L_{amb} for these a-Si,Ge:H alloys. For the 20at.% sample in state A, however, the relatively lower value of $L_{amb} \times TH1^{1/2}$ indicates that other factors also play a significant role in limiting L_{amb}.

Finally, we note that, unlike the ambipolar diffusion lengths, the photoconductivity determined $\eta\mu\tau$ values are not so easily attributed to any of the defect densities we have determined. Further more detailed studies are now being planned to try to elucidate the connection between the $\eta\mu\tau$ values and the electronic structure in the mobility gap.

5.0 CATHODIC AMORPHOUS SILICON-GERMANIUM ALLOYS

5.1 MOBILITY GAP STRUCTURE AND DEEP DEFECT

As described in Section 2, we examined two series of a-Si,Ge:H alloy films deposited by the cathodic glow discharge method at Harvard University onto heavily p^+ doped crystalline silicon substrates. The first series consisted of five samples with Ge fractions in the range 57at.% to 100at.% in increments of 7 to 15at.%. The second series all had Ge fractions near 67at.% but had varying degrees of contamination with an intentional air leak. The results from this second series of samples are described in Section 5.2.

We first carried out drive-level capacitance profiling measurements at 100Hz for a series of temperatures between 290K and 350K to determine the mid-gap defect densities in these cathodic samples. In Fig.15(a) we display typical drive-level capacitance profiling data for the sample with x = 0.57. Unlike the Uni-Solar a-Si,Ge:H samples, the drive-level density, N_{DL}, exhibited very little temperature dependence. For comparison, we plot in Fig. 1(b) the temperature variation of N_{DL} for the Uni-Solar sample in a similar composition range (x = 0.5). There are, we believe, two reasons that N_{DL} might be temperature independent for the cathodic samples. First, the bulk Fermi level E_F^o may be very close to the quasi Fermi level in deep depletion. In this case, we would be probing the entire deep depletion charge density at even the lowest measurement temperature so that N_{DL} already has its maximum value at 320K. Second, there may be a narrow defect band lying at or above E_F^o. In that case the capacitance profiling would only show us the portion of the defect band lying below E_F^o. Thus, the increment of N_{DL} with temperature would be extremely small. Either of these situations imply that we may only be profiling a limited region of the total deep defect band.

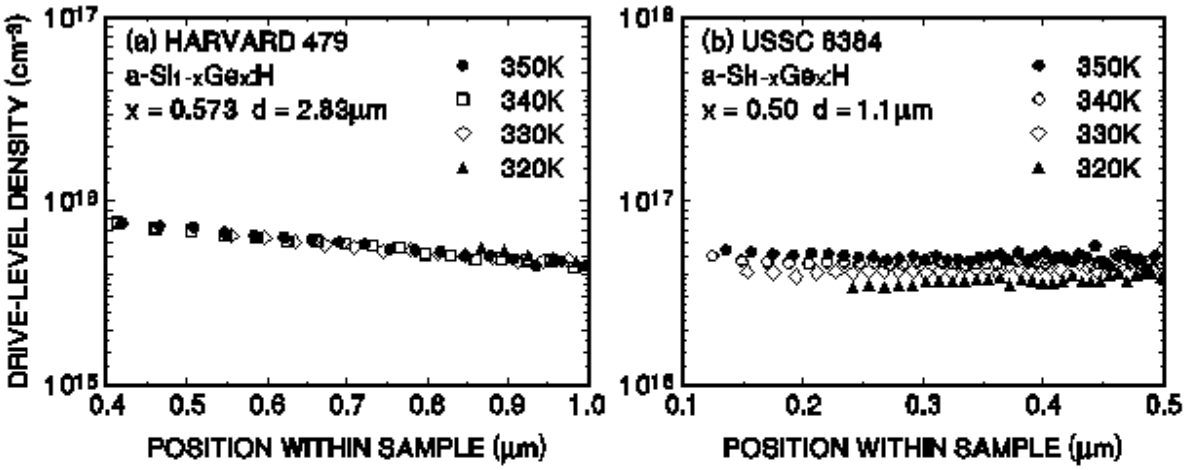

FIG. 15. (a) Temperature independent drive-level density of a cathode deposited sample, (b) an example of the temperature dependent drive-level density of a Uni-Solar sample.

In Fig. 16 we plot the measured values of N_{DL} *vs*. the Ge content determined for these cathodic alloys along with results from our early studies of photo-CVD a-Si,Ge:H samples obtained from the Institute for Energy Conversion (Delaware) [14] and for the Uni-Solar glow discharge samples described in Section 4. For both these previous series of samples we believe that the limiting value of N_{DL} is indeed providing us with an accurate estimate of the total density of the mid-gap defect band. Although N_{DL} for the cathode deposited glow discharge samples is observed to increase with germanium content in a fashion similar to both the IEC and Uni-Solar samples, its value is *almost one order of magnitude lower* than the trend line at high Ge composition indicated for the other a-Si,Ge:H samples.

FIG. 16. . A comparison of the total defect densities vs. Ge content for the a-Si,Ge:H alloys from three sources: photo-CVD samples produced at IEC at University of Delaware [14], glow discharge samples produced at USSC [19,20], and the cathodic glow discharge samples produced at Harvard. The solid symbols are the experimental defect densities determined by DLCP, the open symbols are the defect density estimated from sub-band-gap optical spectra. The dashed lines are the predicted dependence using the spontaneous bond breaking model, assuming E_U is 53 meV and ΔE is 0.3eV for the IEC and USSC samples; and assuming E_U is 45 meV with a larger value of ΔE (0.38eV) for Harvard's samples.

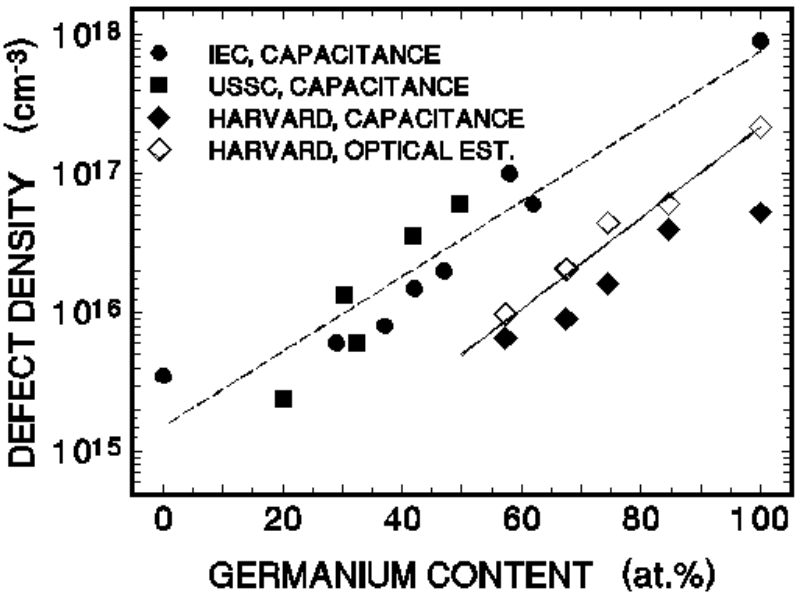

To determine the energy positions of the deep defect bands in the mobility gap, we carried out transient photocapacitance and photocurrent measurements on these samples. In Fig. 17 we compare three photocurrent spectra for the Harvard samples with three such spectra for the Uni-Solar samples. First we note very similar Urbach slopes for both series of samples. We also note the obvious difference in optical gaps due to the different composition ranges for the two sets of samples. However, the Harvard samples have somewhat larger optical gaps than would fit the series for the Uni-Solar samples extrapolated to higher Ge content. There is also a significant difference in the *shape* of the mid-gap absorption due to the deep defects. As we will discuss shortly, this comes about because the cathodic a-Si,Ge:H defect band has a lower optical energy threshold to the conduction band than the Uni-Solar a-Si,Ge:H samples.

Another major difference in the optical spectra is apparent in Fig. 18 where we compare a *pair* of photocapacitance and photocurrent spectra for one Uni-Solar sample (with x=0.50) with one cathodic a-$Si_{1-x}Ge_x$:H sample (with x=0.57) measured under identical conditions. In all of the Uni-Solar samples we observe a significant deviation between the photocapacitance and photocurrent spectra obtained at higher temperatures similar to that shown in Fig. 18(b). As we discussed in Section 3.3 and elsewhere [11,16], the deviation in the bandtail region is due to contribution of hole processes which decrease the relative magnitude of the photocapacitance signal. The additional larger deviation near 1.0eV is due to the excitation of valence band electrons into an unoccupied defect level (OP2) within the mobility gap. In contrast, in Fig. 18(a)

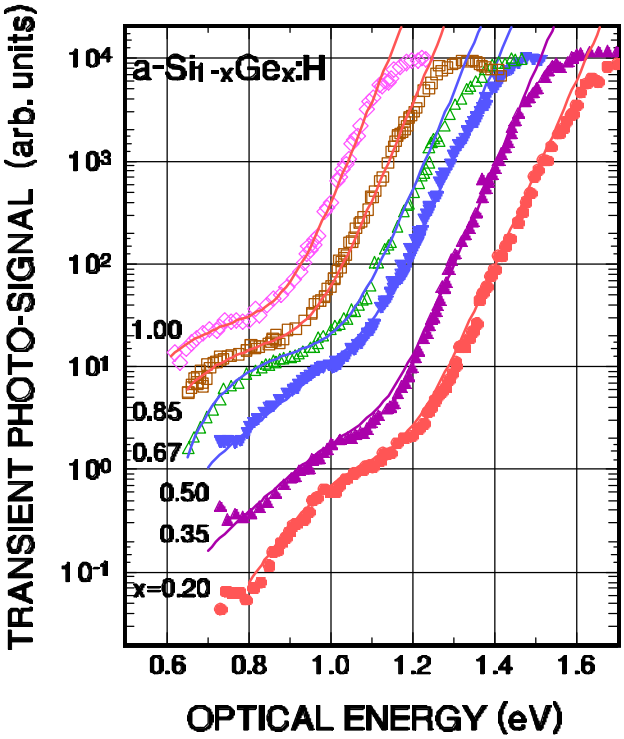

FIG. 17. Transient photocurrent sub-band gap spectra for 3 of the Harvard cathodic glow discharge a-Si,Ge:H samples (open symbols) together with the spectra of 3 of the Uni-Solar a-Si,Ge:H samples (solid symbols). Note that both sets of samples exhibit similar Urbach slopes. However, also note that the deep defect band has a somewhat different appearance for the two sets of samples.

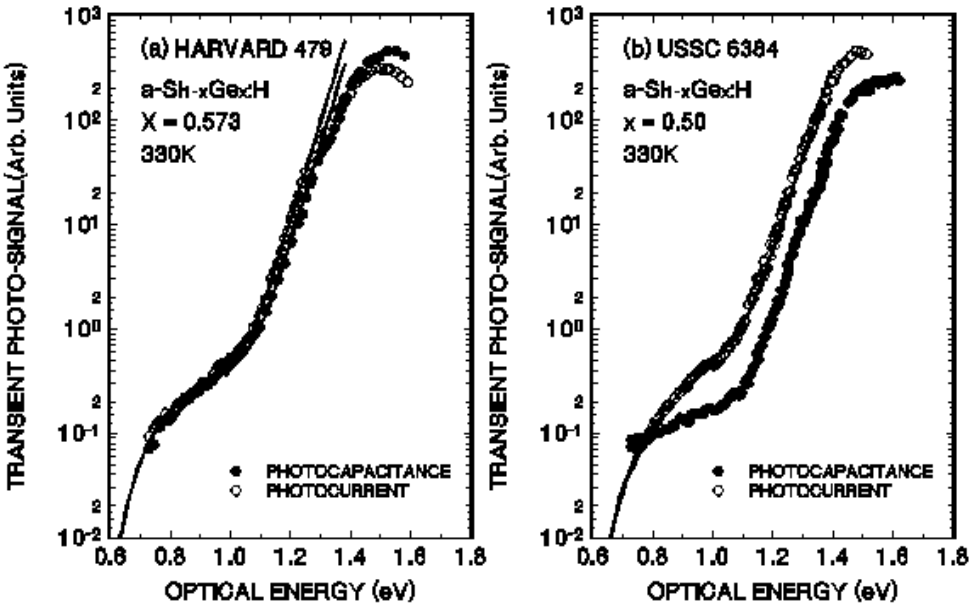

FIG. 18. Pairs of photocapacitance and photocurrent transient spectra for two a-Si,Ge:H samples taken at 330K. These spectra have been aligned to coincide at the lowest optical energies. The marked difference between the two spectra in (b) can be attributed to minority carrier processes.

we find that there is a nearly constant ratio between the photocurrent and photocapacitance spectra for that sample throughout the entire optical energy regime (0.6eV < $h\nu$ < 1.4eV). This means that the displacement of each hole is sufficiently small that it has very little effect on the transient signals. The most straightforward conclusion would be that the hole $\mu\tau$ products for the cathodic a-Si,Ge:H samples are significantly lower than for the Uni-Solar samples.

This interpretation, however, is a bit of an oversimplification. In Section 4.2 we presented a more detailed analysis by which one can estimate the hole $\mu\tau$ products from the ratio, R, of the photocapacitance to the photocurrent signals in the bandtail energy region. This is given by Eq. (6). A close examination of the data for the two samples in Fig. 18 indicates that the ratio, R, in the bandtail region (near 1.2eV) between the photocapacitance and photocurrent signals is roughly 0.1 for the Uni-Solar sample *vs*. 0.6 for the Harvard sample. The charge density in deep depletion, which is given to us directly from our measurement of N_{DL}, is 5×10^{16} cm^{-3} and 6×10^{15} cm^{-3} for the two samples, respectively. Thus we obtain values of $(\mu\tau)_h$ from Eq. (6) of 2.3×10^{-10} cm^2/V for the Uni-Solar sample and 3.2×10^{-10} cm^2/V for the Harvard sample. The error is roughly $\pm$20% in the first case and somewhat larger, $\pm$50%, in the second case (due to difficulty in determining R very accurately when the difference between the spectra is so small). Thus, to within the experimental uncertainty, the $\mu\tau$ products for Harvard samples appears to be quite comparable to those for the Uni-Solar a-Si,Ge:H samples.

However, such a result is nonetheless surprising. The $\mu\tau$ products that we obtain from

this type of measurement are indicative of deep trapping processes since they must limit the escape distance for a carrier on roughly a one second time scale. Thus, if the deep defect density is really nearly an order of magnitude lower, then $\mu\tau$ products should be correspondingly greater. Indeed, in Section 4.2 we showed that the product $(\mu\tau)_h N_D$ is nearly constant in the Uni-Solar samples. It was also found to be nearly constant in our previous studies of photo-CVD a-Si,Ge:H material over an very large range of Ge concentration [14]. Therefore, the comparable values of $(\mu\tau)_h$ for similar Ge content for the cathodic alloy samples really does suggest a fundamental difference in their properties compared to other types of a-Si,Ge:H material.

Figures 17 and 18 taken together display the sub-band-gap spectra for four of the cathodic a-Si,Ge:H samples studied. In all cases there is only a very small difference between the photocurrent and the corresponding photocapacitance spectra. Assuming constant optical matrix elements for bandtail transitions and the deep defect band related transitions we are able to fit the spectra for the cathodic samples using a single Gaussian deep defect band and a valence band tail of constant slope. (We assumed a constant density of states for the conduction band.) Examples of these fits are shown by the thin solid lines drawn through the data points for each curve in Figs. 17 and 18. The Urbach energies deduced in this manner are found to be quite small for these samples, lying close to 45meV in all cases. (For the pure a-Ge:H sample the Urbach energy was determined to be 43meV). From our fitting, we also deduce a broad Gaussian shaped defect band, with width parameter, σ, of 0.2eV, lying about 40meV above the mid-gap energy for each sample.

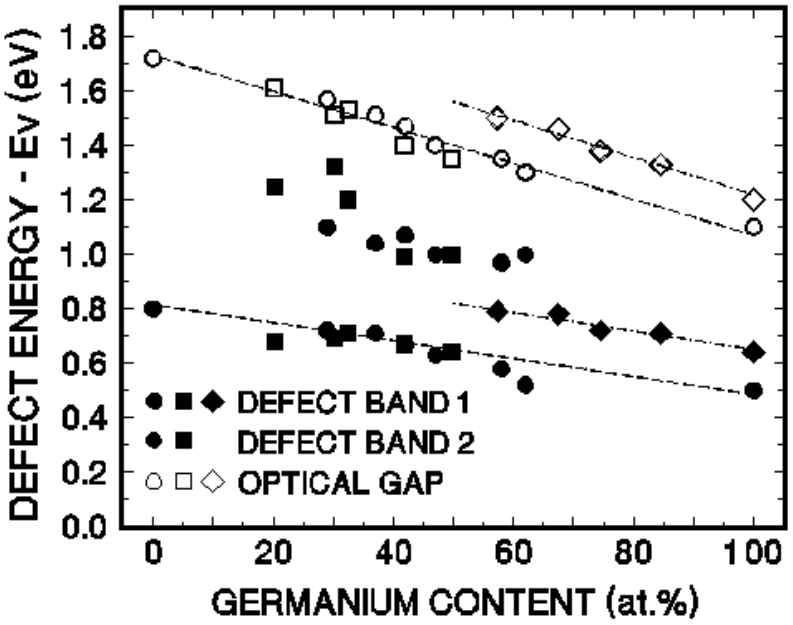

FIG. 19. Energy positions (with respect to E_V) of the defect bands deduced from the sub-band-gap optical spectra for the cathode deposited samples (diamonds) compared with those determined for the IEC photo-CVD samples (circles) [14] and the USSC conventional glow discharge alloy samples (boxes) [19,20]. The optical gaps for each of the samples is also shown for reference [26].

In Fig. 19 we plot the energy positions of this single optical defect band along with the two optical defect bands obtained from fitting the optical spectra for the Uni-Solar samples. (The results for our previous series of the IEC photo-CVD samples have also been included.) As we

discussed above, the second defect transition is not evident in the Harvard samples; however, the minimal hole signal might make the second transition difficult to identify even if it were present. We note that the FWHM of the midgap optical defect band for the cathodic samples is almost twice as large as those of the IEC and Uni-Solar samples and the energy positions are somewhat shallower than those of the IEC and Uni-Solar samples.

These spectra can be employed to help verify the low defect densities obtained for the cathodic samples from the drive-level capacitance profiling measurements discussed above. By normalizing the integral of the deduced Gaussian band with the integral of the valence bandtail states we can assign a total defect density to the optical defect band. We assume that the density of valence bandtail states is the same for all these samples since they all exhibit the same Urbach tail slope and use a value of 2×10^{21} cm^{-3} eV^{-1} for the density of states at the valence band mobility edge. Thus, the integrated number of defect states for the valence bandtail is roughly 10^{20} cm^{-3}. Comparing the integral of the defect band with this value provides our estimate for the total density of deep defects. This method has been applied to optical spectra of pure a-Si:H and provides excellent agreement with defect densities derived from drive-level capacitance profiling for those samples [23,27]. The results of this estimate from the optical spectra are included in Fig. 16. We see that the optical estimates for the cathode deposited samples are higher than their drive-level densities by about a factor of 2. This indicates that the drive-level densities may, indeed, providing us with a slight underestimate of the defect density. However, even the larger optical estimates of the defect densities for these cathode deposited samples are substantially lower than the trend line established for the a-Si,Ge:H samples from the other sources.

Both the drive-level densities and the estimates from optical spectra indicate that the as-grown defect densities increase exponentially with increasing the Ge content in the cathode deposited alloys (see Fig. 16). Such a trend is consistent with the "spontaneous bond breaking" model [28] which has been used successfully to predict the dangling bond defect density in the a-Si,Ge:H samples from the other sources (see the dashed line in Fig. 16) [14,22]. In this model, dangling bonds are thought to be created spontaneously during growth from bandtail states lying beyond a certain demarcation energy above the valence band edge; i.e., "weak bonds". Such a model predicts that the number of dangling bonds will depend solely on the slope of Urbach tail, E_u, and the demarcation energy, E_{db}, relative to the valence band mobility edge. Specifically, if the valence bandtail is described by:

$$N_{tail}(E) = N^{*} exp(-(E-E^{*})/E_u), \qquad (7)$$

where N^{*} @ 10^{21} cm^{-3} is the density of states at $E^{*} \approx E_V + 0.15eV$, then the number of defects created during growth will be:

$$N_D = \int_{E_{db}}^{\infty} N_{tail}(E)dE = E_u N^{*} \exp(-(E_{db} - E^{*}) / E_u) \qquad (8)$$

The value of E_{db} is obtained by subtracting an energy of order the defect half-width (the standard deviation, σ, of the Gaussian distribution describing the defect band) from the energy position of the defect band. From Fig. 19 we can deduce that the defect position vs. Ge content obeys the relation E_D-E_V = $E_{opt}/2$ - *50meV* for the IEC and Uni-Solar samples, and E_D-E_V = $E_{opt}/2$ + *40meV* for the cathode deposited samples. This implies, to a first approximation, that we should have the following relation between defect densities and optical bandgap:

$$N_D = 10^{21} E_u \exp(\Delta E / E_u) \exp(-(E_{opt} / 2E_u)) \qquad (9)$$

where ΔE is equal to E^* - E_V, plus a quantity proportional to the width of the defect band, plus the offset between the defect position and midgap. We found a good agreement with the values of the optical estimates using a ΔE of about 0.38eV, which is slightly larger than its value for the IEC and Uni-Solar samples (in those cases ΔE is about 0.3eV). This difference of about 80 meV for ΔE comes from the different energy positions of the defect band in the mobility gap between the cathode deposited samples and the Uni-Solar (and IEC) samples. We plot the measured vs. the calculated values for N_D in Fig. 20, and also have included the predicted trends as the dashed lines in Fig. 16. It is clear from Fig. 20 that the optical estimates of cathode deposited samples lie on the same trend line as the IEC and Uni-Solar samples. This indicates that the lower defect densities in the cathode deposited samples can be understood within such a model as arising from the different relative position of the defect band within the gap for these samples, their larger optical gap for a given Ge content, and their lower Urbach energies.

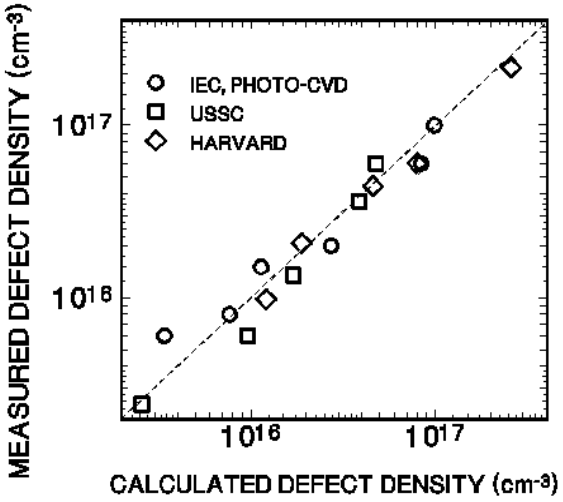

FIG. 20. Measured vs. calculated values of deep defect densities for a-Si,Ge:H alloy samples from various sources. The measured values plotted were obtained from drive-level capacitance profiling except for the cathodic samples where they were estimated from the sub-band-gap optical spectra. The calculated values were obtained from Eq. (9).

Summarizing our experimental results regarding the states in the mobility gap of the Harvard cathodic a-Si,Ge:H alloys, we have found that the main features include: (1) a very small Urbach energy, (2) a single broad deep defect band of optical transitions, and (3) a substantially lower defect density compared to other types of alloys in the Ge-rich composition range. It is tempting to associate such qualities with the superior microstructure recently inferred from small

angle X-rays scattering (SAXS) studies on the cathode deposited alloy samples [29].

5.2 RELATION BETWEEN MINORITY CARRIER TRANSPORT AND DEEP DEFECTS

To investigate the relationship between transport properties and the deep defects in the cathodic PECVD a-Si,Ge:H alloys, we examined a second series of such samples in collaboration with Paul Wickboldt, Dawen Pang, and William Paul of Harvard University (Paul Wickboldt is currently employed at Lawrence Livermore National Laboratory). For these studies four samples were deposited simultaneously on p^+ crystalline Si and 7059 glass substrates with intentional air contamination levels at 0, 2ppm, 10ppm, and 75ppm. All were deposited to yield a Ge fraction of 67at.%. More details concerning the properties of these samples, including the SIMS determined oxygen and nitrogen impurity levels of these four samples, have been given in Section 2. In Table VIII we list the transport properties determined for these samples including the activation energies, E_σ, of conductivity, the photoconductivity determined $\eta\mu\tau$ values, and the ambipolar diffusion lengths determined by SSPG measurements. These dark conductivity, photoconductivity, and SSPG measurements were performed by our collaborators at Harvard on the 7059 glass substrate samples in the dark annealed state (state A) of each sample.

TABLE VIII. Basic transport properties of the air contaminated cathodic a-Si,Ge:H samples in state A.

Sample Number	Air Admixture (ppm)	E_σ (eV)	$\eta\mu\tau$ ($cm^2\ V^{-1}$)	L_{amb} (Å)
523	0	0.68	2.3×10^{-8}	615
525	2	0.64	5.0×10^{-8}	550
524	10	0.64	7.7×10^{-8}	459
526	75	0.58	1.7×10^{-7}	339

TABLE IX. Defect densities determined from drive-level capacitance profiling (DLCP) and from fits to the sub-band-gap spectra for both the dark annealed state (A) and the light soaked state (B). Values of the conductivity activation energies determined from ac admittance measurements and the Urbach bandtail characteristic energy are also listed.

Sample Number	Air Admixture (ppm)	State	E_σ (eV)	DLCP Defect Density (10^{16} cm^{-3})	Optical Spectra Defect Density (arb. units)	Urbach Energy (meV)
523	0	annealed light soaked	0.66 0.63	1.1 2.1	1.5 1.9	43
525	2	annealed light soaked	0.66 0.60	1.3 2.7	1.9 3.6	43
524	10	annealed light soaked	0.66 0.60	1.7 2.0	2.3 2.3	43
526	75	annealed light soaked	0.60 0.58	2.3 3.6	4.0 3.7	45

These samples were then characterized by ac admittance, drive-level capacitance profiling (DLCP), and sub-band-gap photocapacitance and junction photocurrent spectroscopy at the University of Oregon. Samples were examined in both the dark annealed state A as well as a light soaked state (B) obtained after 250 hours of exposure to light at $1.7W/cm^2$ intensity using a 840nm long pass filter. Table IX lists the conductivity activation energies in both states A and B obtained from the ac admittance measurements. We note that there is general agreement between these activation energies in state A and those obtained on the co-planar samples using dc measurements.

Table IX includes the deep defect densities determined from DLCP measurements for both state A and state B. It also lists the defect densities obtained from the analysis of the sub-band-gap photocapacitance and photocurrent spectra, fit to assumed single Gaussian defect distribution and dominant (valence) exponential bandtail distribution. In each case the deduced defect band positions (near E_C - 0.87eV) and widths (a Gaussian width parameter of 0.2eV)were found to be essentially identical for all of the samples. The derived defect densities and the values of the Urbach energy are listed in Table IX. We note that, in general, there is good proportionality between the defect densities estimated from DLCP and the fits to the sub-band-gap spectra, particularly for the dark annealed states of these samples. We note the relatively small increase in the deep defect densities indicated particularly from the optical spectra

estimates. The DLCP data indicate a more consistent increase, but this may be more a result of the Fermi level shift toward shallower energies after light soaking rather than a true increase in the densities of deep defects.

Similar increases in defect density with impurity content have been observed previously [30,31]. These changes are consistent with models that link defect creation to the Fermi level position [32]. The detailed mechanism by which oxygen or nitrogen causes this roughly 0.1eV shift in E_F is unclear. It can be speculated that the incorporation of these atoms act in certain configurations like donors to transfer electrons to neutral defects. This should result in a decrease in electron trapping, an increase in hole trapping, and a shallower Fermi energy, in agreement with the results listed in Table VIII.

In particular, the correlation between the ambipolar diffusion lengths and mid-gap defect density that was identified for the Uni-Solar a-Si,Ge:H in Section 4.2 also appears to be present for these cathodic alloy samples. In Fig. 21(a) we have plotted the ambipolar diffusion lengths for the four samples together with the defect densities obtained from the optical spectra (state A only). If these defects dominate recombination then the former quantity should be inversely proportional to the square root of the defect densities. Thus, in Fig. 21(b) we have plotted the ambipolar diffusion length multiplied by the square root of the determined defect density. Indeed, to within a factor of 1.1, we obtain an essentially constant value. The deviation at the larger contamination levels may indicate the influence of the broader valence bandtail width in these samples. We note that a very similar conclusion is reached if the DLCP determined defect densities are used in place of those obtained from the sub-band-gap optical spectra.

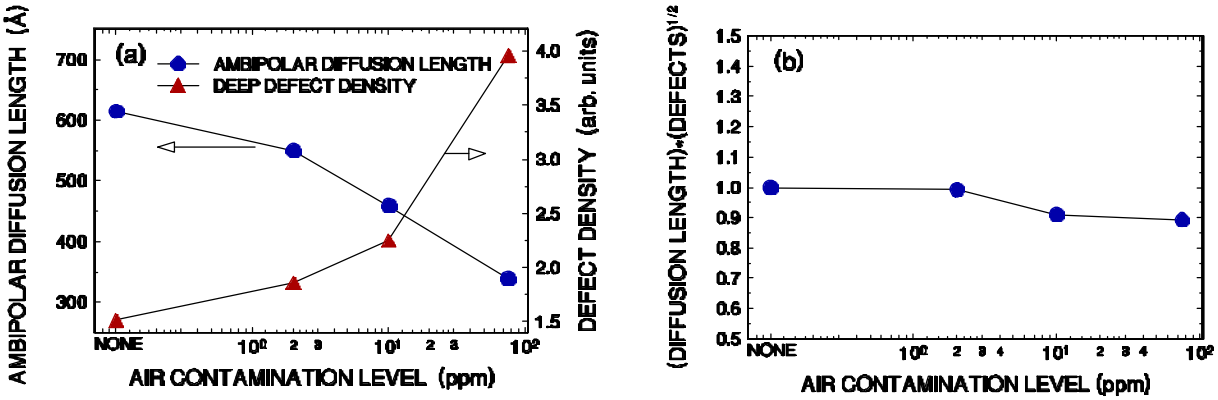

FIG. 21. (a) Variation of the ambipolar diffusion length and the defect density determined from the sub-band-gap spectra *vs.* the air contamination level in the four a-Si,Ge:H samples. **(b)** Product of the ambipolar diffusion length and the square root of the defect density (normalized to be unity for the uncontaminated sample). The nearly constant ratio indicates that the defects dominate the recombination of the holes.

6.0 PROPERTIES OF THE a-Si:H/a-Si,Ge:H HETEROSTRUCTURE INTERFACE

Amorphous silicon (a-Si:H) based multi-junction photovoltaic devices incorporate silicon-germanium alloys (a-Si,Ge:H) for the bottom and/or middle cell. [33,34] It is therefore quite likely that the properties of the a-Si:H/a-Si,Ge:H interface play a key role in determining the performance and the stability of an individual p-i-n cell.[35] In this Section we present results from capacitance transient measurements which disclose a significant concentration of hole traps at this interface. Since hole transport in a-Si:H based solar cells is the limiting factor [36], these results may be quite significant.

The sample configuration used for these measurements have been given in Section 2. A total of eight samples were studied consisting of a thinner (3000-5000Å) layer of a-Si:H next to a thicker layer of a-Si,Ge:H alloy with roughly 35at.% Ge. The opposite side of the a-Si:H layer was contacted either with a heavily doped p+ crystalline Si substrate or a metal Schottky barrier. Thus, the resulting a-Si:H/a-Si,Ge:H heterojunction was positioned within 3000-5000Å of either the Schottky barrier or substrate junction so that its electronic properties could be probed capacitively. The capacitance transient measurements described below were carried out at a temperature of 370K.

We applied a filling pulse to place the junction nearest to the a-Si:H/a-Si,Ge:H interface into forward bias and then recorded the capacitance transients after restoring the initial reverse bias. Under these pulsing conditions all the samples, except those in which the interface was adjacent to the Schottky barrier (i.e., samples 2 and 4), exhibited a particular type of capacitance transient. As displayed in Fig. 22, the transients can be divided into two time regimes: a short time regime, in which the capacitance increases with time corresponding to a *loss* of negative charge (electron-emission type), and a long time regime, in which the capacitance decreases with time corresponding to a *gain* of negative charge (hole-emission type). If the filling pulse voltage

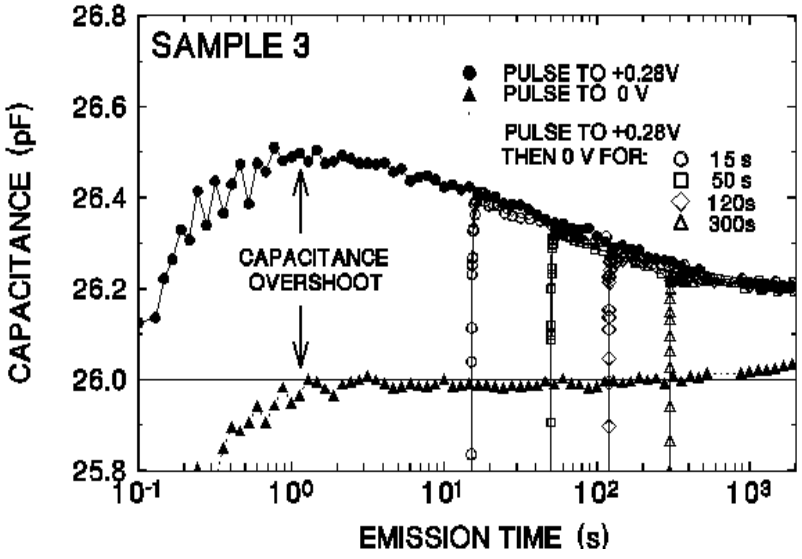

FIG. 22. Capacitance *vs.* time following a 300s long voltage filling pulse to +0.28 volts (solid circles) or to zero volts (solid triangles). The ambient bias was -3V. The four transients denoted with open symbols were again obtained using a 300s filling pulse to +0.28 volts, but were immediately followed by a 0V waiting period of 15s, 50s, 120s, and 300s, respectively. The zero of time for these latter curves corresponds to the end of the +0.28 volt filling pulse.

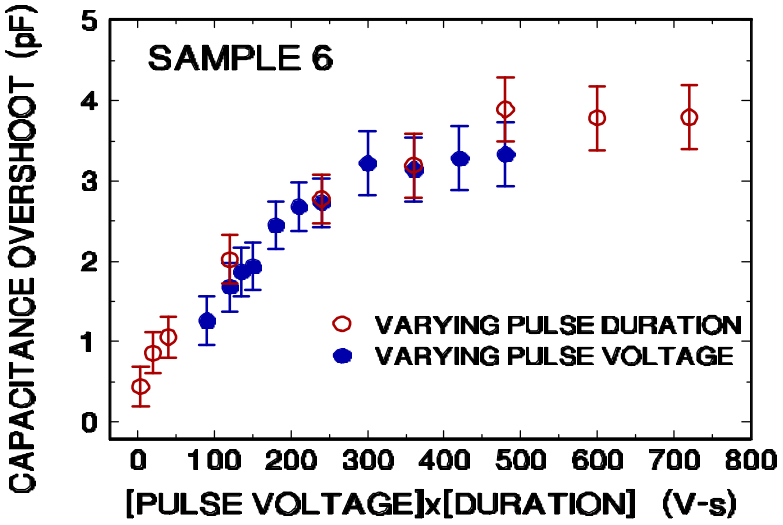

FIG. 23. Capacitance overshoot *vs.* the *product* of the filling pulse voltage (V_p) and the filling pulse duration (t_p) for sample 6 at 370 K. Pulse durations covered the range 10s to 1800s for a fixed 0.4V pulse voltage, and pulse voltages were varied between 0.3V to 1.6V for a fixed 300s pulse duration. The ambient reverse bias was -1.0 volts.

is zero or slightly *negative* (i.e. still in reverse bias), the long time, hole-emission type behavior is not observed. This suggests that hole injection from p^+-silicon is a necessary condition for the occurrence of this second type of transient. Also, the absence of the hole-emission type transients for the forward biased Schottky barrier contacts (samples 2 and 4), where no hole injection can occur, strongly supports this conclusion. We denote the *difference* between the peak capacitance during the transient and the pre-pulse capacitance as the "capacitance overshoot". Figure 23 plots the capacitance overshoot of sample 6 versus the *product* of the filling pulse voltage (V_p) and the filling pulse duration (t_p). We see that the overshoot increases until the $V_p \times t_p$ product reaches a value of about 400 V-s and then saturates. Thus, the maximum number of states/traps that can be filled by the holes is well defined. This allows unambiguous comparisons between trap densities for different samples.

We can demonstrate that the capacitance overshoot transients are due to traps at the heterojunction interface. Beyond a few volts of reverse bias, V_b, the depletion region will extend through the a-Si:H layer and the a-Si:H/a-Si,Ge:H interface into the a-Si,Ge:H alloy. Hence, Poisson's equation can be integrated to obtain [8]

$$V_b = \frac{1}{\varepsilon}\int_0^d x\rho_{\text{a-Si:H}}(x)dx + \frac{Q_{\text{int}}d}{\varepsilon} + \frac{1}{\varepsilon}\int_d^W x\rho_{\text{a-Si,Ge:H}}(x)dx, \qquad (10)$$

where ε is the (average) dielectric constant, x is the distance from the barrier, ρ(x) is the charge density, d is the thickness of a-Si:H layer, W is the total depletion width (using the abrupt depletion approximation) and Q_{int} is the a-Si:H/a-Si,Ge:H interface charge density. After the filling pulse is removed the depletion width at time t, W(t), varies from its pre-pulse value, W_i. Since the bias voltage is restored to its pre-pulse value after the filling pulse, we have

$$\Delta V_b = 0 = \frac{1}{e}\int_0^d x\Delta r_{\text{a-Si:H}}(x)dx + \frac{\Delta Q_{\text{int}}(t)d}{e} + \frac{1}{e}\int_d^{W(t)} x r_{\text{a-Si,Ge:H}}(x)\,dx \; - \frac{1}{e}\int_d^{W_i} x r_{\text{a-Si,Ge:H}}(x)\,dx, \quad (11)$$

provided we neglect the charge emission within a-Si,Ge:H layer. This is reasonable in the long-time limit in which we observe these transients. If we further neglect the charge emission within the a-Si:H layer in this time regime, then the first integral vanishes and the interface charge density can be written as

$$\Delta Q_{\text{int}}(t) = \frac{e^2 A^2 r^{\text{ave}}_{\text{a-Si,Ge:H}}}{2d}\left[\frac{1}{C_i^2} - \frac{1}{C(t)^2}\right], \quad (12)$$

where A is the active area, $r^{\text{ave}}_{\text{a-Si,Ge:H}}$ is the average charge density in a-Si,Ge:H, and we have used the relations $C_i \approx \frac{eA}{w_i}$ and, $C(t) \approx \frac{eA}{W(t)}$, for the initial capacitance and the capacitance at time t, respectively. According to this analysis, if the capacitance transients are dominated by the emission of interface charge, then the right hand side of Eq. (12) should be independent of the applied bias provided it is large enough to allow complete depletion of the interface traps.

Figure 24(a) provides a comparison of the capacitance overshoots for sample 7 as a function of time for different values of the ambient bias under otherwise identical pulsing conditions. The calculated interface charge density from Eq. (12) corresponding to these transients is shown in Fig. 24(b). The value of $r^{\text{ave}}_{\text{a-Si,Ge:H}}$ for each sample was obtained from drive-level capacitance profiling [7] within the a-Si,Ge:H layer (in this case $r^{\text{ave}}_{\text{a-Si,Ge:H}} \approx 2\times 10^{16}$ cm^{-3}). The close overlap of these curves indicates that the charge emission is indeed occurring from within a very localized spatial region.

A comparison of the interface charge densities for samples 5 and 6 obtained under saturation conditions is shown in Fig. 25. According to Table III, these two samples are identical except for the a-Si:H/a-Si,Ge:H interface treatment. From drive-level measurements, we find that the density of states for the a-Si,Ge:H layer in both samples 5 and 6 is nearly identical (about 1.5×10^{16} cm^{-3}) while their deduced trap densities are substantially different. Since the only difference between these two samples was their interface preparation, this verifies that the observed traps are located very close to the interface. In Table X we have listed the saturation values of the interfacial trap densities for the samples studied. For samples 1 and 3, the transients were not recorded under conditions of complete saturation, so the actual trap densities are probably larger than the values listed in the Table.

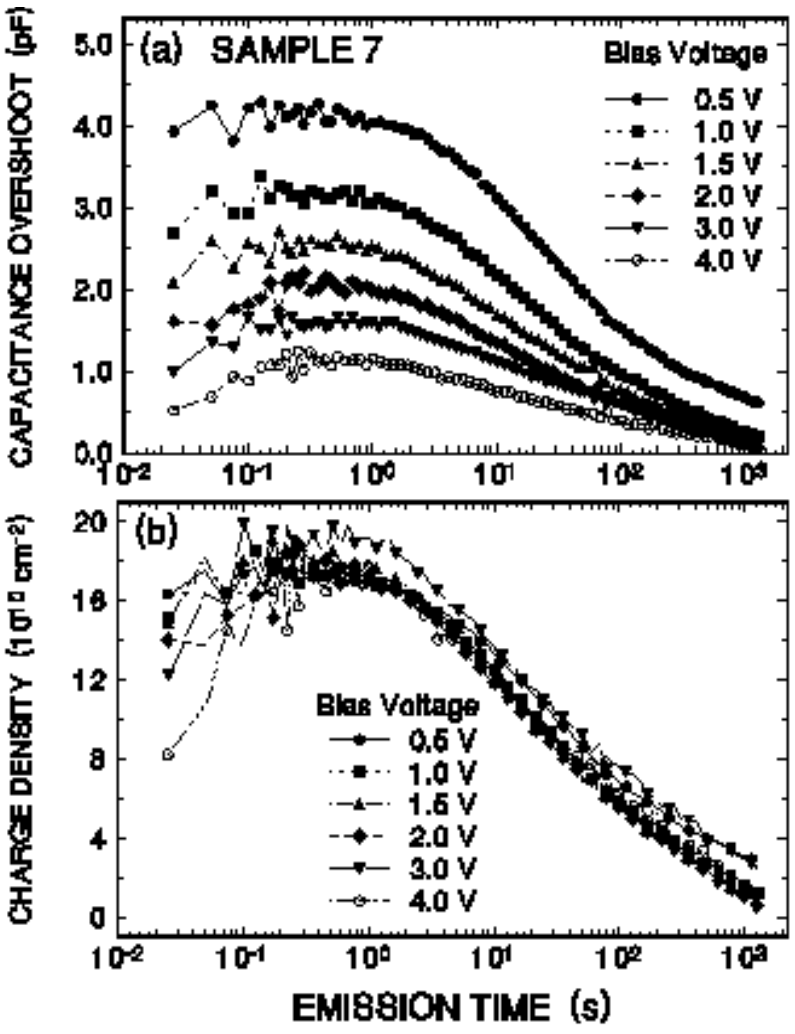

FIG. 24. (a). Capacitance transients for sample 7 using the same 1.6 volt, 300s filling pulse, but using different ambient bias voltages as indicated. **(b)** Calculated interface trap density derived using Eq. (6) for each transient in (a). The close overlap of these different curves confirms that the dominant traps are confined to a particular spatial location (the heterojunction interface).

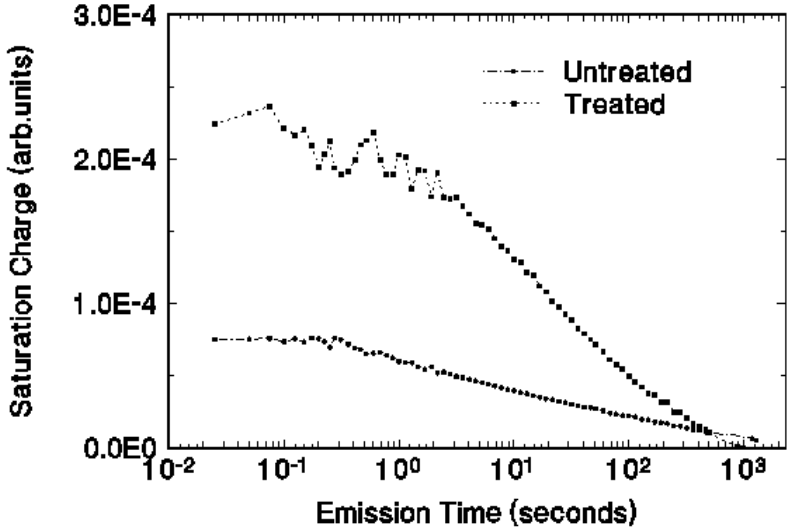

FIG. 25. Charge transients deduced from capacitance transient measurements on a-Si:H/a-Si,Ge:H hetero-junction samples. The magnitude of the areal density of holes traps depends upon the type of interface preparation proce-dure that is employed.

TABLE X. Summary of deduced interface trap densities for a-Si,Ge:H/a-Si:H samples.

#	Sample Configuration	Interface	Q_{int} (cm^{-2})
1	a-Si:H | a-Si,Ge:H	Untreated	$> 1 \times 10^{11}$
2	a-Si,Ge:H | a-Si:H	Untreated	Not observed
3	a-Si:H | a-Si,Ge:H	Untreated	$> 4 \times 10^{10}$
4	a-Si,Ge:H | a-Si:H	Untreated	Not observed
5	a-Si:H | a-Si,Ge:H	Untreated	6×10^{10}
6	a-Si:H | a-Si,Ge:H	Treated	1.6×10^{11}
7	a-Si:H | a-Si,Ge:H	Graded (250 Å)	1.8×10^{11}
8	a-Si:H | a-Si,Ge:H	Graded (1000 Å)	7×10^{10}

To examine the role of these traps in carrier recombination processes, we modified the timing sequence of the transients as follows: At the end of the filling pulse, the sample was held at zero bias for a certain period before the reverse bias was restored to produce the transients. This allowed an increased density of electrons to be present at the heterojunction interface. The transients recorded with these pulsing conditions for sample 3 are included in Fig. 22, where the time at zero bias has been added to the elapsed emission time. The excellent overlap of these curves indicates that the hole emission kinetics are not affected by the presence of the extra electrons. This means that the interface states are not acting as recombination centers for electrons. Also, because the charge emission continues in an identical manner in the absence of an electric field, this eliminates the possibility that the transients arise from polarization effects.

The transients for sample 8, in which the a-Si:H/a-Si,Ge:H interface was graded very gradually over 1000 Å, are qualitatively similar to the other samples. However, the capacitance at long times after the filling pulse does not return to its pre-pulse value even after raising the sample to higher temperature (~ 420 K). This suggests a metastable change in the state of the sample. If a subsequent filling pulse is applied, the resultant transient again indicates a trap density the same as for the prior transients. Since the only difference between sample 8 and sample 7 is the distance over which the interface is graded, this indicates that such metastable changes in the charge state of the traps result from the broader spatial extent of the interfacial region in sample 8. Also, in case of sample 8, the maximum number of traps that can be occupied and subsequently

emptied is considerably smaller than that in sample 7 (See Table X).

While it is clear that the concentration of these traps is determined by the interface preparation during growth, we should also note that, in the deposition of all of these films, the plasma was interrupted between the a-Si:H layer and the a-Si,Ge:H layer. It is nonetheless more likely that these traps are inherent to the interface than a result of plasma interruption. Since the holes at these interface traps do not recombine with electrons, devices incorporating these interfaces may not be too adversely impeded. However, at levels of 10^{11} cm^{-2}, trapped interface charges will significantly alter the electric field profiles in such devices and thus affect the quantum efficiencies. Therefore, the control of these interfacial trapping states appears to be essential for device optimization.

7.0 HOT-WIRE DEPOSITED AMORPHOUS SILICON

Several groups have now reported device-quality a-Si:H films produced by the hot-wire growth technique.[3,37,38] We characterized the electronic properties of a series of NREL deposited hot-wire a-Si:H using transient photocapacitance spectroscopy and also by drive-level capacitance profiling. A comparison of the transient photocapacitance spectra for three hot-wire samples with very different hydrogen levels is displayed in Fig. 26. We then followed the same procedure as described in Sections 4 and 5 for the a-Si,Ge:H alloy studies: We fit the sub-band-spectra to a density of states consisting of an exponential band tail with slope E_U plus a Gaussian shaped deep defect band. The results of these fits are shown as the thin solid lines in Fig. 26. In all cases the deep defect band was located at an energy of 0.85eV below E_C with a width parameter, σ, of 0.18eV.

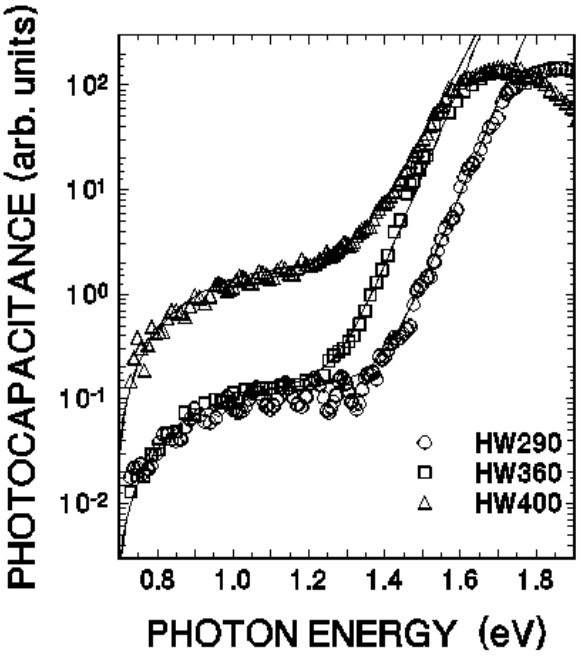

FIG. 26. Comparison of the transient photocapacitance spectra in the as-grown state for three different substrate temperatures. All spectra were obtained at 340K. The solid lines indicate spectra calculated from a density of states consisting of a Gaussian shaped defect band plus an exponential bandtail.

These data clearly indicate a significant reduction in the optical gap for the samples grown at higher substrate temperatures. A value of E_{04} was estimated from the fall off of the signal at higher optical energies which indicated the degree of attenuation of the probe light through the thickness of the sample. These values, together with the derived Urbach energies are summarized in Fig. 27. We see that the Urbach energy remains roughly constant until the hydrogen content falls below 2at.% while, at the same time, the optical gap is decreased by more that 0.1eV. This indicates that a significant reduction in optical gap can be achieved without introducing excess structural disorder into these hot-wire samples.

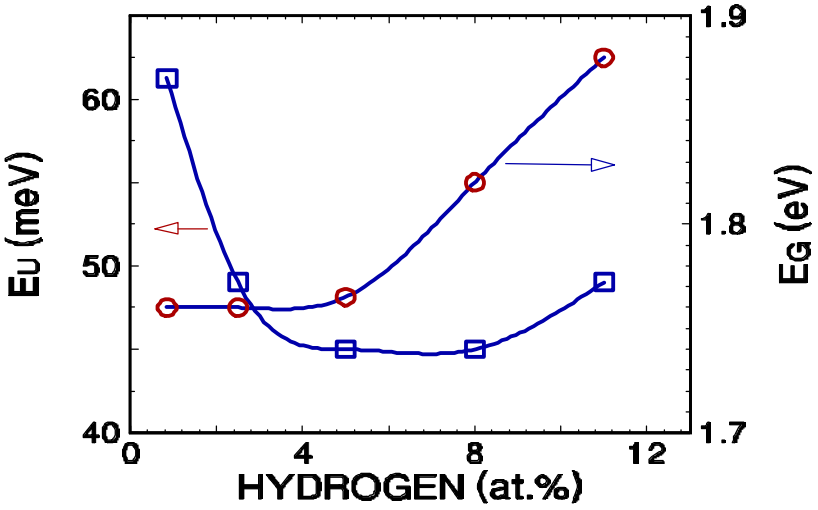

FIG. 27. Variation of the optical gaps and the Urbach energies vs. Hydrogen content determined from the sub-band-gap photocapacitance spectra for the hot-wire a-Si:H samples.

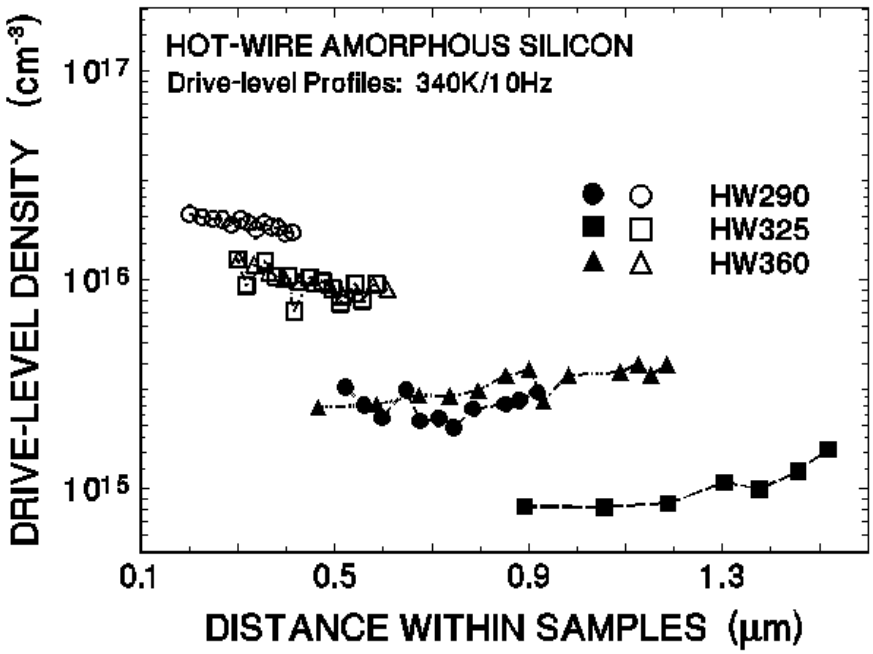

FIG. 28. Drive level capacitance profiling data for three hot-wire a-Si:H samples before (solid symbols) and after (open symbols) light soaking. These data were obtained at 340K using a measurement temperature of 340K. The indicated drive-level profiling densities should be multiplied by a factor of 2 to obtain an estimate of the total deep defect density.

In Fig. 28 we present the results of capacitance profiling measurements on three hot-wire samples with hydrogen content between 2.5 to 12at.% (the lowest H sample was too defective to be measured in this fashion). Results are shown both for the as-grown states and after 110 hours of light soaking at 5 Watts/cm^2 unfiltered tungsten-halogen light. The sample with 2.5at.% H was also examined after 250 hours exposure with no apparent difference, indicating that saturation conditions have been reached. In Fig. 29 we summarize the deduced defect densities in the as-grown state both for the capacitance measurements and also as estimated from the defect band region of the optical spectra obtained from Fig. 26. We find good agreement in all cases where both types of measurements could be performed. This indicates that the estimate of 1.5×10^{17} cm^{-3} defects from the optical spectrum for the lowest H sample is probably fairly accurate. Such a large defect density is certainly not surprising for a sample with less than 1at.% H. However, it is quite surprising that the sample with roughly 2.5at.% H should exhibit a total defect density of less than 1×10^{16} cm^{-3}.

In Fig. 30 we compare the defect densities for the samples before and after light degradation. This figure indicates that the stabilized density of deep defects is actually lowest for the sample near 2.5at.% even though its initial defect density is slightly higher. In general we can state that the highest H sample actually exhibits properties nearly identical to conventional glow discharge a-Si:H while the hot-wire samples with H levels near 2at.% exhibit slightly superior properties: a lower stabilized defect density plus a narrower Urbach edge. Given the fact that these samples also exhibit a slightly lower optical gap, they seem potentially quite promising for incorporation into cells as a superior midgap material.

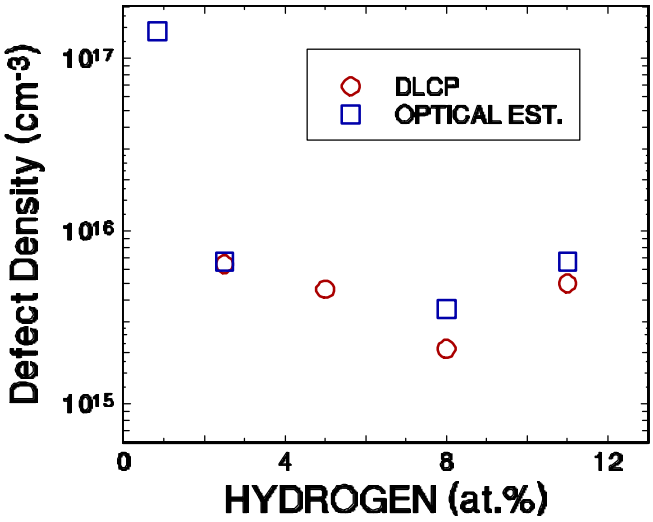

FIG. 29. Comparison of the total deep defect densities obtained both from the capacitance profiling data of Fig. 27 (obtained by doubling the values of the DLCP data at 340K), and the sub-band-gap photocapacitance spectra of Fig. 26. Note the good agreement between the estimates from these two types of experimental data.

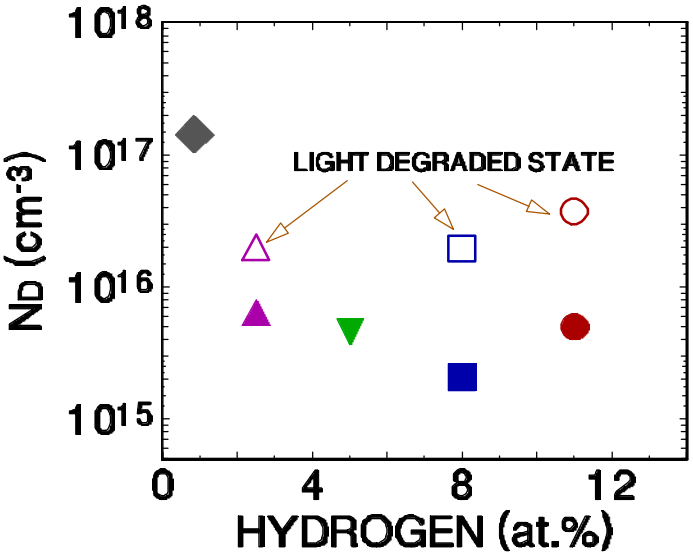

FIG. 30. Comparison of defect densities before (solid symbols) and after light soaking (open symbols). Note that these data indicate that the best stabilized properties are realized for hot-wire samples containing less than 5 at.% hydrogen.

Finally, in Fig. 31 we compare the photocapacitance and photocurrent spectra of HW360 in both State A and State B. As discussed in Section 3 and 4 above, whenever there is an appreciable minority carrier contribution to the motion of charge, the photocurrent signal will be larger than photocapacitance signal. This occurs because the photocapacitance signal is proportional to the *difference* between the electrons and holes that escape from depletion region while the photocurrent signal is proportional to the *sum*. As also discussed in Section 4, we can estimate a value for the hole mu-tau product, $(\mu\tau)_h$, from the ratio of photocapacitance signal to the photocurrent signal in the band tail region [16]. For State A, where there is a clear difference

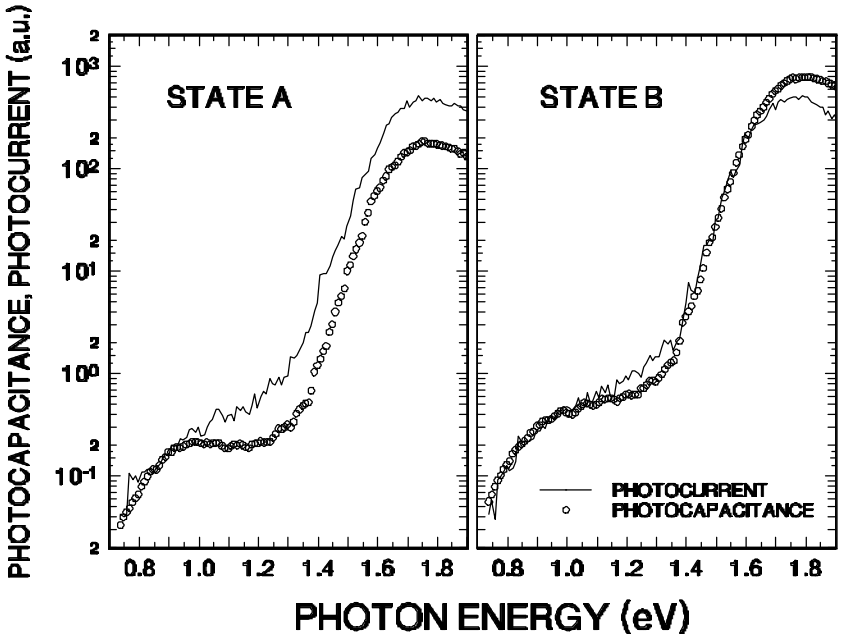

FIG. 31. Photocapacitance and transient photocurrent spectra for sample HW360 in its annealed and light-soaked states. Once the two types of spectra have been aligned in the low optical energy regime, their separation in the bandtail region provides an estimate for the $\mu\tau$ product of the hole. The fact that two types of spectra exhibit very little separation in State B thus indicates a low value of $(\mu\tau)_h$ for this sample in its degraded state.

between the two spectra in the bandtail region we get about 2.4×10^{-9} cm^2/V. However, in state B the difference between photocapacitance and photocurrent signals nearly vanishes. This indicates that the hole mobility decreases markedly after the sample has been degraded. This suggests that, in spite of the quite small increase in deep defect density for the low hydrogen hot wire a-Si:H samples with light soaking, the performance of photovoltaic devices may nonetheless exhibit serious degradation due to this apparent dramatic decrease in $(\mu\tau)_h$.

8.0 STABILITY OF HYDROGEN DILUTED GLOW DISCHARGE a-Si:H

In this Section we present preliminary studies of the effects of hydrogen dilution on the stability of glow discharge a-Si:H with respect to light-induced deep defect creation. The most comprehensive set of samples for these types of studies in my laboratory were produced at Lawrence Berkeley Laboratory (LBL). Therefore, these results are reported first and a comparison will be made between samples deposited with hydrogen dilution vs. helium dilution vs. no dilution. Next we report the results for two samples received from Solarex, one deposited under hydrogen dilution and one deposited with no hydrogen dilution. Finally, we report results for a series of three samples deposited in-house: one deposition under hydrogen dilution, one diluted in argon, and one in which the dilutant gas was modulated between hydrogen and argon. Additional specific information on the growth conditions for all three sets of samples has been given in Section 2 above.

8.1 PROPERTIES OF LBL a-Si:H DEPOSITED WITH HYDROGEN OR HELIUM DILUTION

For this first series of samples, we carried out a comparison study between a-Si:H grown by the glow discharge method either with 100% silane, or with silane diluted in H_2 or He gas. The samples were obtained through collaboration with V. Perez-Mendez group at Lawrence Berkeley Laboratory [39], and further details concerning the growth conditions of these a-Si:H samples are given in Section 2.5. The purpose of this study was actually two-fold: First we wanted to evaluate the reliability of our capacitance characterization methods for n-i-p device structures by directly comparing the results using such a device structures with a single i-layer a-Si:H film deposited on doped crystalline Si with Pd Schottky contacts [denoted below as p^+(c-Si)-i-m, our usual sample configuration for capacitance measurements], and also with a-Si:H deposited on n^+ a-Si:H on top of Cr coated glass with Schottky contacts at the top surface [denoted as n-i-m]. Second, we wanted to compare the electronic properties, particularly the stability properties, of hydrogen diluted, helium diluted, and undiluted glow discharge deposition.

Samples were characterized by drive-level capacitance profiling (DLCP) measurements as described in Section 3. An example of the profiles obtained for one H_2 diluted n-i-p sample (Sample 1) at a series of measurement temperatures is shown in Fig. 32. Typically, a good estimate of the total deep defect density is obtained by doubling the profile value for the 100Hz, 400K case. Such an estimate has been found to agree quite well with ESR spin densities for a-Si:H samples.[23] For this sample, this implies a deep defect density of only 9×10^{14} cm^{-3}. By the same method, the defect density for the standard sample (undiluted discharge) is determined to be 3×10^{15} cm^{-3}, which agrees quite well with previously measured high quality glow discharge samples.

Next, we repeated measurements on some samples using the n-i-m or the p^+(c-Si)-i-m configurations. A couple examples of such comparisons are displayed in Fig. 33 where we have plotted the spatially averaged DLCP values at several temperatures for two samples each with different contacting configurations. In all cases the DLCP values are *identical to within a factor of 1.25,* independent of the contacts. Thus the DLCP defect densities appear to uniquely reflect the properties of the i-layer in each sample.

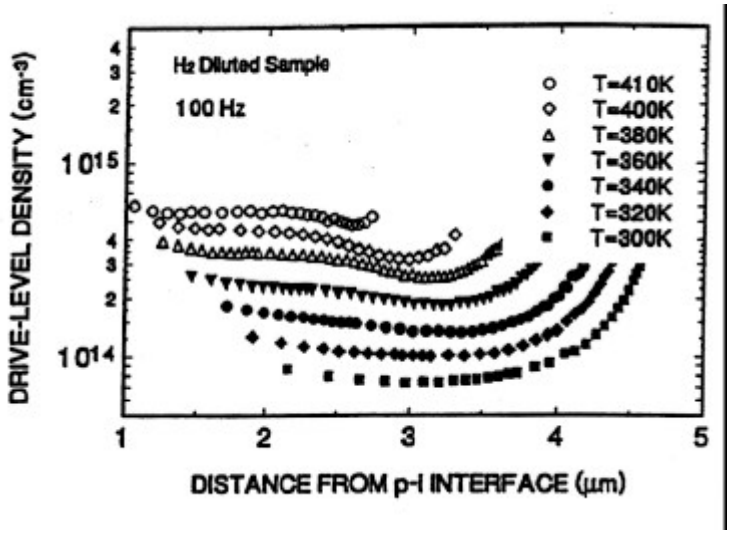

FIG. 32. Example of 100Hz drive-level capacitance profiling data measured for a series of fixed temperatures for sample 1. A good estimate for the total deep defect density is obtained from doubling the drive-level density for the 400K profile.

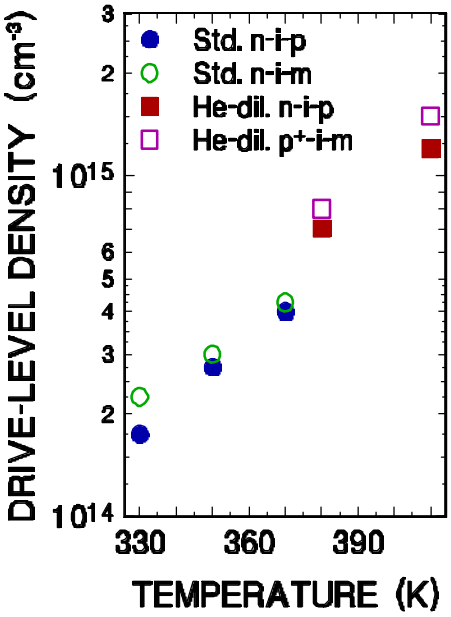

FIG. 33. Comparison of drive-level densities (spatially averaged) for different contacting configurations for two types of a-Si:H films.

TABLE XI. Carrier mobilities and deep defect densities for samples in their dark annealed states. The TOF mobility measurements were carried out at LBL.

Sample	Dilutant Gas	μ_e (cm^2/V)	μ_h (cm^2/V)	N_D (cm^{-3})
1	H_2	4.2	0.013	9×10^{14}
2	H_2	2.8	0.009	1.0×10^{15}
3	H_2	2.3	0.006	9×10^{14}
4	He	1.2	0.003	1.0×10^{15}
5	He	0.7	0.004	2.2×10^{15}
6	none	1.0	0.004	2.8×10^{15}

The electron and hole mobilities were determined for these samples at LBL using the standard time-of-flight (TOF) technique. A summary of the determined values for μ_e and μ_p are listed in Table XI for the annealed state of each of the six samples. The values of defect densities we determined by DLCP are also included. The DLCP measurements were carried out at 100Hz at a measurement temperature of 410K. We see that the hydrogen diluted samples show improved transport properties for both electrons and holes and, correspondingly, a greatly reduced deep defect density when compared to either the He or standard glow discharge samples.

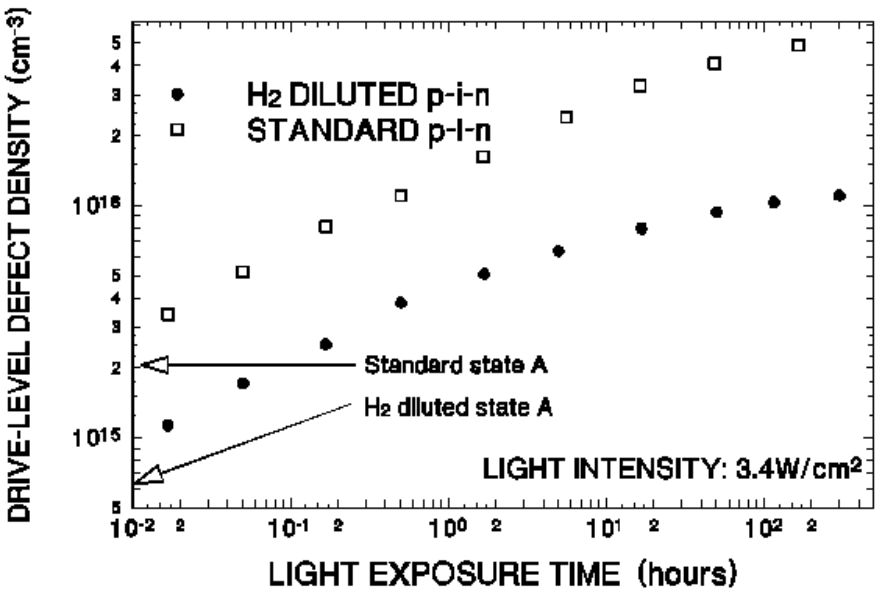

FIG. 34. Comparison of drive-level determined defect densities for sample 1 and sample 6 as a function of light exposure. The total defect densities are estimated by multiplying these drive-level values by a factor of 1.5.

Finally, we compared the light-induced degradation of one hydrogen diluted sample (sample 1) with the standard sample (sample 6). Both samples were exposed for up to 300 hours to a 1.9eV red filtered tungsten-halogen light source at an intensity of 3.4 W/cm^2. The samples were immersed in methanol during light soaking to maintain their surface temperatures below 65^{o}C. We display the drive-level profiles obtained at a measurement temperature of 370K and a frequency of 10 Hz as a function of light exposure in Fig. 34. Here we see a substantially lower degraded defect density in the hydrogen diluted sample at each exposure, as well as much earlier saturation in that case. Ultimately, *the hydrogen diluted sample exhibits at least a factor of five improvement compared to the standard glow discharge a-Si:H sample*. Further measurements to test the degraded properties of the remaining samples are in progress.

8.2 PROPERTIES OF SOLAREX a-Si:H DEPOSITED WITH HYDROGEN DILUTION

We also carried out one preliminary study of Solarex a-Si:H samples grown with and without hydrogen dilution. We evaluated the degraded defect densities in these two samples using both of our standard methods: via drive-level capacitance profiling and by photocapacitance spectroscopy. Both samples were light soaked for 90 hours at 400mW/cm^2 before evaluation.

Results from the capacitance profiling measurements are shown in Fig. 35 and those from photocapacitance are shown in Fig. 36. Both measurements indicate that the hydrogen diluted sample degraded to a deep defect density that was nearly a factor of 2 lower than the normal glow discharge a-Si:H film. That is, the Solarex hydrogen diluted material definitely appears to be more stable against light induced defect formation than conventional glow discharge a-Si:H.

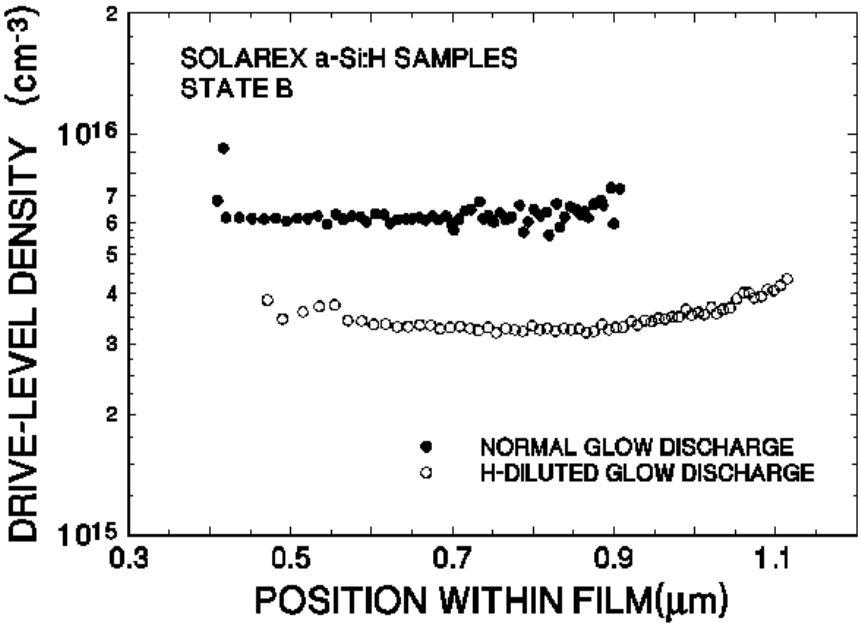

FIG. 35. Drive-level deep defect profiles for two a-Si:H samples in light-degraded states. These 500Hz capacitance profiles measured at 360K should be multiplied by a factor of 3 to yield an estimate of the total defect density [23]. The sample grown with hydrogen dilution shows a significantly lower concentration of defects.

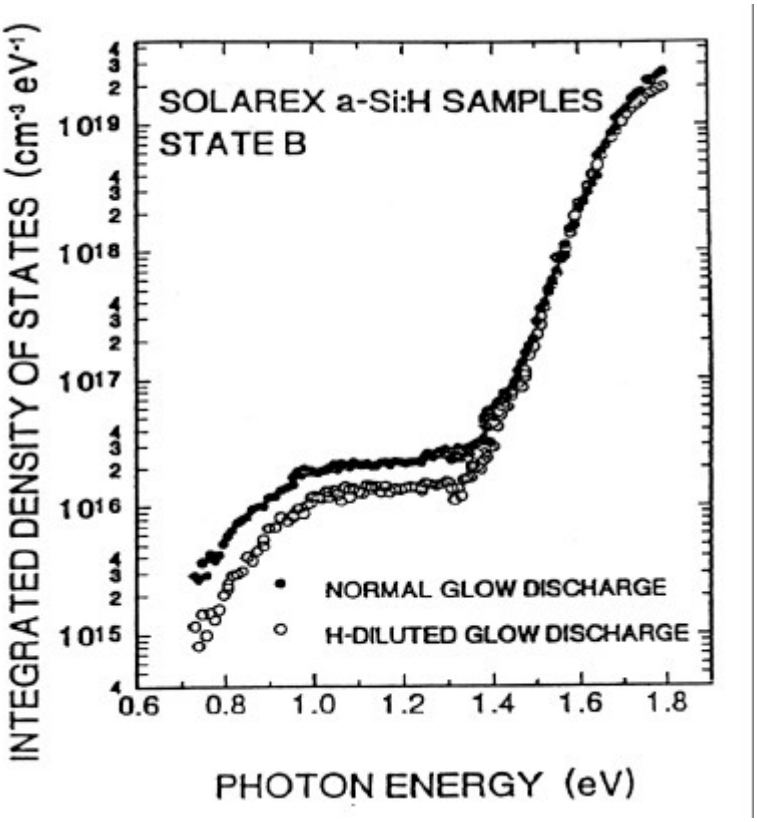

FIG. 36.
Photocapacitance sub-band-gap spectra for the same two samples in their light-degraded states. The difference in magnitudes of the deep defect portion of these spectra agrees with that indicated in the drive-level profiling measurements shown above.

8.3. POSSIBLE MECHANISMS: HYDROGEN DILUTION MODULATION STUDIES

In order to gain some insight into the possible mechanisms responsible for the above decrease in susceptibility to the light-induced degradation for the hydrogen diluted material we attempted a somewhat unique approach. We tried to examine the differences in degradation between hydrogen diluted and normal material *within a single a-Si:H film.*

To evaluate this kind of approach we deposited three kinds of a-Si:H films on heavily doped p^+ crystalline silicon substrates by the RF glow discharge technique at 200 °C: One was a multilayer sample and the other two were homogeneous samples. One homogeneous sample was deposited from a mixture of silane and argon gases and the other from a mixture of silane and hydrogen gases. Each layer in the multilayer sample was grown from the silane gas diluted alternately with either argon or hydrogen gas. The dilution ratio of the silane gas to the total gas mixture for all cases was identical such that the silane gas accounted for 30 % of the volume fraction of the total gas flow. Each argon (hydrogen) dilution layer in the multilayer sample was grown for 15 (10) minutes with a total of 34 layers in all for a total growth time of 7 hours and 5 minutes. This resulted in a 4 μm thick sample, giving a modulation period of about 2300 Å.

After the growth, palladium Schottky barriers were evaporated on top of the amorphous films. A series of light soaked states were obtained by exposing the samples to about 400 mW/cm^2 band gap light for a determined period of time at each step. Following more than 100 hours of light soaking, and saturation of the deep defect densities, a series of partially annealed states were attained by annealing the samples at a series of increasing temperatures for 10 minutes duration at each temperature. Final post-annealed states were obtained by annealing the samples for 30 minutes at 520 K (the same temperature for preparing the initial state A samples).

The spatial dependence of the defect densities were examined by our drive-level capacitance profiling method. Figure 37 shows such data for several different states for the three samples. We observe that the multilayer sample shows a clear variation in its defect densities vs. distance in state A and also after short light exposure times (up to about 1 hour). The spatial period is exactly what we expected from the modulated growth conditions. Moreover, the high defect value of multilayer sample matches the value of the homogeneous hydrogen diluted sample and the low value of multilayer sample matches the value of homogeneous argon diluted sample. This means that hydrogen dilution sample has higher density of defects than the argon diluted sample in state A and so does hydrogen diluted layer in multilayer sample.

However, as the illumination time gets longer the defect level of hydrogen diluted homogeneous sample becomes almost the same as the defect level of argon diluted homogeneous sample and the variation of defect of multilayer sample becomes very small. This can be seen in the 5.33 hours illumination data in Fig. 37. This behavior is distinct from what we had observed in the Lawrence Berkeley and Solarex samples and indicates that the growth conditions for our samples did not match theirs in some significant way. Obviously, this study should be repeated with higher hydrogen dilution conditions. Nonetheless, we can state that the high and low densities of defects of multilayer sample track well those defect levels of homogeneous samples until the time of light soaking reaches around 11 hours.

Following this level of light exposure, however, something quite unexpected happens. More prolonged light soaking causes the defect level of multilayer sample to become larger than *either* of the homogeneous samples! Moreover, the higher defect density condition of the multilayer sample persists until the samples are annealed at high temperatures. Only when the multilayer sample is fully annealed (at the same temperature as the original state A) do the defect levels show a clear match to the levels of the fully post-annealed hydrogen diluted sample and that of the argon diluted sample.

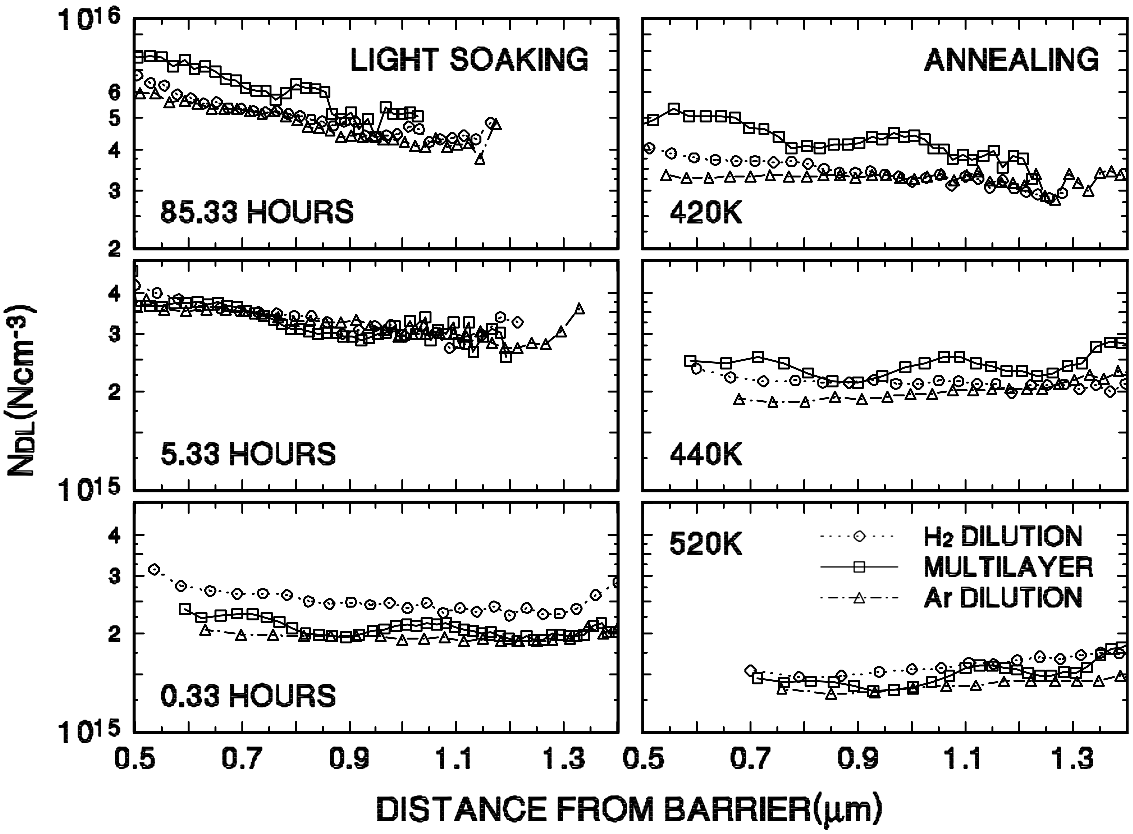

FIG. 37. Drive-level capacitance profiling data for three light soaked states (left) and three post-annealed states (right). The times shown in the left figures are light soaking times and the temperatures shown in the right figures are post-annealing temperatures. Chronologically the left bottom figure is the earliest state and the sequence progresses in a clockwise fashion.

The data presented above are relatively unique in that they allow us to begin to distinguish between local and global aspects of light induced defect creation and annealing. "Local" aspects would be those that are controlled by characteristics of the individual sites for stable and metastable defects and their immediate surroundings: non-diffusing impurities, voids, complexes, etc. Examples of "global" aspects would be those that are controlled by free carrier densities, impurities that are able to diffuse over distances comparable to the multilayer distance, and film strain.

Such local aspects also seem to dominate the metastable defect creation in the earlier stages of light soaking. Unfortunately, because the homogeneous Ar and H_2 diluted films have defect levels which become very similar after a few hours exposure, we cannot be sure whether or not this local character persists. Since carrier recombination is a dominant factor in creating these metastable defects, one would expect to observe a more global aspect to the metastable defect densities; namely, that the multilayer defect density would tend to become more uniform after long periods of light exposure. We will be able to test this in more detail in the future by

utilizing component layers whose susceptibility to light induced degradation in homogeneous films exhibit a more pronounced difference.

The most surprising aspect of the defect creation process in our multilayer sample is that the defect density at long light exposure times eventually *exceeds* that of either homogeneous film. This is difficult to understand simply in terms of local or global equilibrium processes. To account for such a result we must identify mechanisms that are peculiar to the multilayer nature of that sample. At present we can offer two possibilities: First, that it involves the separation of free electron and hole carriers and, second, that it is related to an increased level of strain in the multilayer sample. The first of these seems less likely for two reasons: separating holes and electrons should tend to reduce the rate of metastable defect creation. In addition, such a mechanism might be expected to accentuate the differences between the light-induced effects in the different layers.

The second mechanism, that a multilayer sample may have intrinsically a high degree of strain than a homogeneous film of either type, seems more plausible. Indeed, studies relating metastable defect creation to film strain in a-Si:H were reported nearly a decade ago.[40] However, if this is indeed the correct explanation it is then a bit surprising that the state A defect densities do not seem to be affected since these quite accurately reproduce the levels in each of the homogeneous samples. Such a result implies a very different character to the stable vs. the metastable defects and thus seems to contradict a fundamental assumption of defect equilibrium models. Along these lines it is also noteworthy how well the final post-annealing treatment restores the spatial defect variation of the initial state. This again implies a definite local aspect for the stable defects independent of any changes that have occurred as a result of prolonged light exposure and annealing (such as diffusion of H between the layers).

9.0 STUDIES OF ELECTRON-CYCLOTRON-RESONANCE DEPOSITED a-Si:H.

The final component in our effort to evaluate new, potentially more stable forms of a-Si:H was a study of a series of several a-Si:H samples produced by an electron cyclotron resonance (ECR) growth method. These films were deposited at Iowa State University (under the direction of Vikram Dalal) onto stainless steel substrates. All of them incorporated an n^+ a-Si:H layer at the substrate contact and each i-layer was roughly 1.5μm thick. Palladium Schottky barrier junctions were evaporated onto the top surface to allow characterization by our junction capacitance methods. For this study the methods included drive-level capacitance profiling, to determine deep defect densities, plus transient photocapacitance measurements, to determine the sub-band-gap optical spectra. Samples were evaluated in their as-grown condition and also after 50 hours of light soaking at an intensity of $4W/cm^2$ using red filtered ELH light.

Figure 38 gives an example of sub-band-gap spectra obtained by our transient photocapacitance measurements for one ECR sample (deposited using H_2 dilution) before and after light soaking. Such spectra allow us to deduce the characteristic energy of the Urbach edge (56meV in this case) and also the ratio of deep defect increase due to light induced degradation (roughly a factor of 2). They can also be used to obtain a rough estimate of the total defect density; however, a more quantitative value is obtained from our capacitance profiling measurements. Table XII summarizes the results for the 3 ECR grown a-Si:H samples whose characterization has now been completed. Two of the samples listed were grown with H_2 dilution and one was deposited with He dilution. All samples exhibited properties comparable to glow discharge grown a-Si:H films, although with somewhat higher degraded defect densities than hydrogen diluted material obtained by the latter method. We should mention, however, that because the ECR samples studied were deposited onto textured substrates, there may exist some uncertainty of the actual sample area. This could result in a substantial overestimate in the defect densities listed since these vary inversely with the *square* of the assumed sample areas. Also, the ECR growth conditions are still being varied to achieve optimum material properties. Therefore,

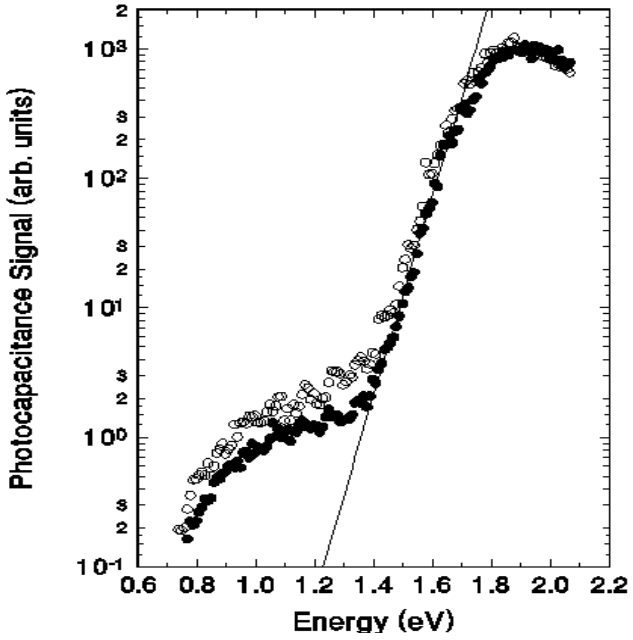

F**IG. 38.** Photocapacitance sub-band-gap spectra for a H_2 diluted ECR deposited a-Si:H sample in its as-grown state (solid symbols) and after 50h of intense light degradation (open symbols). The solid line indicates the slope of the Urbach tail which is 56meV for this sample.

TABLE XII. Summary of preliminary results for ECR a-Si:H film properties.

Sample (dilution)	E_U (meV)	E_σ (eV) state A	E_σ (eV) state B	N_D (cm^{-3}) state A	N_D (cm^{-3}) state B
1779 (H_2)	56	0.61	0.71	$3.1\pm0.2x10^{16}$	$6.5\pm0.5x10^{16}$
1780 (H_2)	52	0.66	0.75	$2.2\pm0.2x10^{16}$	$4.8\pm0.3x10^{16}$
1793 (He)	52	0.68	0.76	$1.3\pm0.2x10^{16}$	$3.2\pm0.3x10^{16}$

the results presented in this report should be regarded as only a first look at this potentially promising new kind of mid-gap amorphous material.

10.0 SUMMARY AND CONCLUSIONS

The work carried out for our NREL Subcontract has been focused on the characterization and evaluation of low gap (a-Si,Ge:H) alloy materials or on issues related to overall stability in the mid-gap (a-Si:H) materials. In many cases our studies have focussed on such materials produced using novel deposition methods and/or conditions. We also made a detailed study of the interface between these two materials in a-Si:H/a-Si,Ge:H heterostructures. One series of a-Si,Ge:H alloy samples and the heterostructure samples were obtained through an ongoing collaboration with United Solar Systems Corporation, while another series of a-Si,Ge:H alloy "cathodic" samples were deposited through a collaboration with workers at Harvard University. Our studies of the a-Si:H samples, produced under a wide variety of deposition conditions were obtained in collaboration with researchers at NREL for hot-wire deposited material, with Iowa State for ECR deposited samples, and several sources for a-Si:H grown under hydrogen dilution: Lawrence Berkeley Laboratory, Solarex, as well as some in-house samples. A couple additional series of hydrogen diluted a-Si:H samples were also obtained; however, these studies are not yet in a sufficient stage of completion for their inclusion in this report.

First of all, the results from our Uni-Solar a-Si,Ge:H studies represent a continuation of our attempts to fully understand the electronic properties of the device quality low-gap alloys. Previously we had identified at least one type of defect band transition in these alloys that did not seem to be present in pure a-Si:H and had hypothesized that it could correspond to a significant population of D^+ states in the nominally intrinsic a-Si,Ge:H alloy material. The light induced degradation studies also seemed to support this conclusion and, furthermore, indicated that charged defect ratios can vary significantly after light soaking. Additional studies then examined the properties of very lightly n- and p-type a-Si,Ge:H material. The results on these samples verified that charged defects are indeed responsible for the different observed defect bands in

device quality a-Si,Ge:H alloy material. This conclusion undoubtedly will have important consequences for understanding the transport and degradation process in a-Si,Ge:H devices.

Second, we reported results of our measurements on a-Si,Ge:H alloy "cathodic" samples produced at Harvard University. These samples were found to exhibit significantly lower defect densities in the high Ge composition range (>50at.% Ge) than alloy samples produced either by conventional glow discharge or photo-CVD deposition. Moreover, this lower defect density appears to be entirely consistent with simple defect formation models given the differences observed for other aspects of the electronic structure in these samples: a larger gap energy for a given Ge fraction, a different relative energy position of the defect within the gap, and a smaller Urbach energy. It is as yet unclear, however, whether these cathodic alloy samples will lead to a significant improvement in low gap cells. That is, our measurements also indicated a much smaller value of $(\mu\tau)_h$ for these samples than would have been expected given their lower defect densities. Nonetheless, these cathodic alloys do potentially appear to be quite promising.

Third, we performed voltage pulse stimulated capacitance transient measurements on a-Si:H/a-Si,Ge:H heterostructure samples to look for carrier trapping states that might be associated with this interface. We found that, for filling pulses that put the interface into forward bias, there was a clear signature of trapped hole emission extending over long times. Furthermore, we were able to confirm that these hole traps were associated specifically with the interface itself in concentrations of roughly 10^{11} cm^{-2}. We found that treatment or grading of the interface modified the concentrations of these hole traps; however, they did not seem to act as recombination centers for electrons brought into the interface region. Nonetheless, these traps seem to exist in sufficient densities to significantly alter the electric field profiles across such heterojunction structures and, therefore, they are likely to significantly impact the performance of tandem and triple cells which incorporate such interfaces.

Next, we reported our results on several hot-wire a-Si:H samples produced with varying hydrogen levels. These samples were evaluated in both their as-grown state as well as a strongly light degraded state. We found that samples with a H content above 10at.% exhibited essentially identical properties to those of conventional glow discharge a-Si:H. However, as the H level was decreased to about 2at.% the electronic properties actually *improved*: the degraded defect level was reduced and the Urbach tail was slightly narrower. These changes were accompanied by more than a 0.1eV decrease in optical gap. Therefore, our studies indicate that hot-wire produced a-Si:H, with H levels between 2-5at.%, should lead to mid-gap devices with superior properties.

Finally, we discussed some results on glow discharge material as well as ECR deposited a-Si:H grown under hydrogen dilution conditions. We confirmed that, in terms of deep defect creation, such films exhibited improved stability compared to conventional glow discharge

material: roughly a factor of three lower deep defect densities than those grown using pure silane. Furthermore, the hydrogen diluted samples degraded at a slower rate and saturate at a significantly lower value (by about a factor of five) than pure silane deposited sample. These results agree with reports of increased relative stability of cells employing hydrogen-diluted i-layers. We also began some studies to try to gain some insight into the mechanisms responsible for such differences in stability. We compared Ar and H samples with a sample that was switched periodically between these two types of gas mixtures during growth. While still very preliminary, our studies point to film strain as playing a primary role for the observed differences in behavior.

11.0 SUBCONTRACT SUPPORTED PUBLICATIONS

Daewon Kwon and J. David Cohen, "Metastable Defect Studies in hydrogen modulated multilayer amorphous silicon", Mat. Res. Soc. Symp. Proc. **336**, 305 (1994).

F. Zhong, J.D. Cohen, J. Yang, and S. Guha, "The electronic structure of a-Si,Ge:H alloys", Mat. Res. Soc. Symp. Proc. **336**, 493 (1994).

F. Zhong, C.-C. Chen, J.D. Cohen, P. Wickboldt, and W. Paul, "Defect properties of cathode deposited glow discharge amorphous silicon germanium alloys", Mat. Res. Soc. Symp. Proc. **377**, 553 (1995).

D. Kwon, J.D. Cohen, B.P. Nelson, and E. Iwaniczko, "Effect of light soaking on hot wire deposited a-Si:H films", Mat. Res. Soc. Symp. Proc. **377**, 301 (1995).

F. Zhong, C-C. Chen, and J.D. Cohen, “Electronic structure and light induced degradation of amorphous silicon-germanium alloys”, J. Non-Cryst. Solids, **198-200**, 572 (1996).

P. Wickboldt, D. Pang, W. Paul, J.H. Chen, F. Zhong, J.D. Cohen, Y. Chen, and D.L. Williamson, “Improved a-$Si_{1-x}Ge_x$:H of large x deposited by PECVD”, J. Non-Cryst. Solids, **198-200**, 567 (1996).

C. Palsule, J.D. Cohen, U. Paschen, “Capacitance characterization of amorphous silicon/ amorphous silicon-germanium heterostructures”, Mat. Res. Soc. Symp. Proc. **420**, 209 (1996).

C-C. Chen, F. Zhong, J.D. Cohen, “Effects of light induced degradation on the distributuion of deep defects in hydrogated amorphous silicon-germanium alloys”, Mat. Res. Soc. Symp. Proc. **420**, 581 (1996).

F. Zhong, W.S. Hong, V. Perez-Mendez, C.-C. Chen, and J.D. Cohen, “The electronic properties of a-Si:H deposited with hydrogen or He dilution”, Mat. Res. Soc. Symp. Proc. **420**, 363 (1996).

C. Palsule, U. Paschen, J.D. Cohen, J. Yang, and S. Guha, “Evidence for hole traps at the amorphous silicon/silicon-germanium heterostructure interface”, Appl. Phys. Lett. **70**, 499 (1997).

B. von Roedern, K. Zweibel, E. Schiff, J.D. Cohen, S. Wagner, S.S. Hegedus, and T. Peterson, “Progress Report on the Amorphous Silicon Teaming Activities”, AIP Conf. Proc. **394**, 3 (1997).

Paul Wickboldt, Dawen Pang, William Paul, Joseph H. Chen, Fan Zhong, Chih-Chiang Chen, J.David Cohen, and Don L. Williamson, “Recent improvements in glow discharge a-$Si_{1-x}Ge_x$:H of large x”, J. Appl. Phys. **81**, 6252 (1997).

B. von Roedern, E. Schiff, J.D. Cohen, S. Wagner, and S.S. Hegedus, “Summary of 4 1/2 years of research experience of the U.S. amorphous silicon research teams”, Progress in Photovoltaics:

Research and Applications **5**, 345 (1997).

Chih-Chiang Chen, Fan Zhong and J. David. Cohen, Jeffrey C. Yang And Subhendu Guha, “The significance of charged defects in understanding the light-induced degradation of hydrogenated amorphous silicon-germanium alloys”, Mat. Res. Soc. Symp. Proc. **467**, 55 (1997).

D. Kwon, J.D. Cohen, and R. Garcia, “An AFM study of the effect of growth method and conditions on the microstructure of a-Si:H”, Mat. Res. Soc. Symp. Proc. **467**, 561 (1997).

Paul Wickboldt, Dawen Pang, William Paul, Joseph H. Chen, Chih-Chiang Chen, and J.David Cohen, “Ambipolar phototransport ($\mu\tau_e = \mu\tau_h$) observed as an intrinsic property of a-Si,Ge:H”, Mat. Res. Soc. Symp. Proc. **467**, 263 (1997).

Chih-Chiang Chen, Fan Zhong, J.D. Cohen, Jeffrey C. Yang, and Subhendu Guha, “Evidence for charged defects in intrinsic glow discharge hydrogenated amorphous silicon-germanium alloys”, Physical Review B(Rapid)**57**, R4210 (1998).

12.0 REFERENCES

1. S. Guha, J.S. Payson, S.C. Agarwal, and S.R. Ovshinsky, J. Non-Cryst. Solids **97-98**, 1455 (1988).

2. W. Paul, J. Non-Cryst. Solids **137&138**, 803 (1991).

3. A.H. Mahan, J. Carapella, B.P. Nelson, and R.S. Crandall, J. Appl. Phys. **69**, 6728 (1991).

4. Lang, D.V., Cohen, J.D., and Harbison, J.P., Phys. Rev. B**25**, 5285 (1982).

5. C.E. Michelson, A.V. Gelatos, and J.D. Cohen, Appl. Phys. Lett. **47**, 412 (1985).

6. K.K. Mahavadi, K. Zellama, J.D. Cohen, and J.P. Harbison, Phys. Rev. B**35**, 7776 (1987).

7. Lang, D.V. in *Thermally Stimulated Relaxation in Solids*, vol. 37 of Topics in Applied Physics, ed by P. Braunlich (Springer, Berlin, 1979), p. 93.

8. Cohen, J.D., in *Hydrogenated Amorphous Silicon*, vol. 21C of Semiconductors and Semimetals, ed. by J. Pankove (Academic Press, New York, 1984), p. 9.

9. Gelatos, A.V., Cohen, J.D., and Harbison, J.P., in *Optical Effects in Amorphous Silicon*, ed. by P.C. Taylor and S.G. Bishop (AIP Conf. Proc. No. 120, New York, 1984), p. 16.

10. Gelatos, A.V., Cohen, J.D., and Harbison, J.P., Appl. Phys. Lett. **49**, 722 (1986).

11. Cohen, J.D., and Gelatos, A.V., in *Amorphous Silicon and Related Materials*, ed. by H. Fritzsche (World Scientific, Singapore, 1989), p. 475.

12. Amer, N.M., and Jackson, W.B., in *Hydrogenated Amorphous Silicon*, vol. 21B of Semiconductors and Semimetals, ed. by J. Pankove (Academic Press, New York, 1984), p. 83.

13. Vanacek, M., Kocka, J., Stuchlik, J., Kozisek, Z., Stika, O., and Triska, A., Sol. Energy Mat. **8**, 411 (1983).

14. T. Unold, J.D. Cohen, and C.M. Fortmann, Appl. Phys. Lett. **64**, 1714 (1994).

15. J.D. Cohen and A.V. Gelatos, ref. 11, pp. 475-512.

16. J.D. Cohen, T. Unold and A.V. Gelatos, J. Non-Cryst. Solids **141**, 142 (1992).

17. A.V. Gelatos, K.K. Mahavadi, and J.D. Cohen, Appl. Phys. Lett. **53**, 403 (1988).

18. T. Unold, J.D. Cohen, and C.M. Fortmann, J. Non-Cryst. Solids **137&138**, 809 (1991).

19. C. C. Chen, F. Zhong and J. D. Cohen, Mat. Res. Soc. Symp. Proc. **420**, 581 (1996)

20. C. C. Chen, F. Zhong and J. D. Cohen, J.C. Yang, and S. Guha, Mat. Res. Soc. Symp. Proc. **467**, 55 (1997).

21. This is confirmed by measuring the sign of the photocurrent for short wavelength light.

22. F. Zhong, J.D. Cohen, J.C. Yang, and S. Guha, Mat. Res. Soc. Symp. Proc. **336**, 493 (1994).

23. T. Unold, J. Hautala, and J.D. Cohen, Phys. Rev. B**50**, 16985 (1994).

24. Note: This expression is in a slightly corrected form from what had appeared in Refs. 14, 15, and 17.

25. S. Aljishi, Z E. Smith, and S. Wagner, in *Amorphous Silicon and Related Materials*, ed. by H. Fritzsche (World Scientific, Singapore, 1989), p. 887.

26. For the cathode deposited samples we used an optical gap of E04 minus 60meV. The corresponding values of the optical gap for the IEC and USSC samples were estimated from their transient photocurrent spectra.

27. D. Kwon, J.D. Cohen, B.P. Nelson, and E. Iwaniczko, Mat. Res. Soc. Symp. Proc. **377**, 301 (1995).

28. M Stutzmann, Philos. Mag. B**60**, 531 (1989).

29. D. L. Williamson, Y. Chen., and S.J. Jones, AIP Conf. Proc. **124**, 442 1994).

30. S. Tsuda, et. al. Jap. J. Appl. Phys. **26**, 33 (1987).

31. H. Haku, et. al., Jap. J. Appl. Phys. **26**, 1978 (1987).

32. B. Ebersberger and W. Krühler, Appl. Phys. Lett. **65**, 1683 (1994).

33. J. Yang and S. Guha, Appl. Phys. Lett. **61**, 2917 (1992).

34. S. Guha, J. Yang, A. Banerjee, T. Glatfelter, K. Hoffman, S.R. Ovshinsky, M. Izu, H.C. Ovshinsky, and X. Deng, Mat. Res. Soc. Symp. Proc. **336**, 645 (1994).

35. S. Guha, J. Yang, A. Pawlikiewicz, T. Glatfelter, R. Ross, and S.R. Ovshinsky, Appl. Phys. Lett. **54**, 2330 (1989).

36. R.R. Arya, M.S. Bennett, K. Rajan, and A. Catalano, Appl. Phys. Lett. **55**, 1894 (1989).

37. P. Papadopoulos, A. Scholz, S. Bauer, B. Schröder, and H. Oechsner, J. Non-Cryst. Solids **164-166**, 87 (1993).

38. E.C. Molenbroek, A.H. Mahan, E.J. Johnson, and A.C. Gallagher, Mat. Res. Soc. Symp. Proc. **336**, 43 (1993).

39. Samples from Lawrence Berkeley Laboratory are courtesy of F. Zhong, W.S. Hong, and V. Perez-Mendez.

40. M. Stutzmann, W.B. Jackson, and C.C. Tsai, J. Non-Cryst. Solids **77&78**, 363 (1985).

REPORT DOCUMENTATION PAGE

Form Approved
OMB NO. 0704-0188

1. AGENCY USE ONLY (Leave blank)	2. REPORT DATE	3. REPORT TYPE AND DATES COVERED
	November 1998	Final Subcontract Report, 18 April 1994–15 January 1998

4. TITLE AND SUBTITLE
Identifying Electronic Properties Relevant to Improving Stability in a-Si:H-Based Cells and Overall Performance in a-Si,Ge:H-Based Cells; Final Subcontract Report, 18 April 1994–15 January 1998

5. FUNDING NUMBERS
C: XAN-4-13318-07
TA: PV905001

6. AUTHOR(S)
J.D. Cohen

7. PERFORMING ORGANIZATION NAME(S) AND ADDRESS(ES)
Department of Physics and Materials Science Institute
University of Oregon
Eugene, OR 97403

8. PERFORMING ORGANIZATION REPORT NUMBER

9. SPONSORING/MONITORING AGENCY NAME(S) AND ADDRESS(ES)
National Renewable Energy Laboratory
1617 Cole Blvd.
Golden, CO 80401-3393

10. SPONSORING/MONITORING AGENCY REPORT NUMBER
SR-520-25802

11. SUPPLEMENTARY NOTES
NREL Technical Monitor: B. von Roedern

12a. DISTRIBUTION/AVAILABILITY STATEMENT
National Technical Information Service
U.S. Department of Commerce
5285 Port Royal Road
Springfield, VA 22161

12b. DISTRIBUTION CODE

13. ABSTRACT *(Maximum 200 words)*

The work carried out by the University of Oregon under this subcontract focused on the characterization and evaluation of low-gap (a-Si,Ge:H) alloy materials and on issues related to overall stability in the mid-gap (a-SiH) materials. First, researchers characterized an extensive series of Uni-Solar a-Si,Ge:H samples using drive-level capacitance profiling and the analysis of sub-band-gap photocapacitance and photocurrent spectra. Thus, several bands of deep defect transitions were identified. Researchers were able to verify that charged defects are responsible for the different observed defect bands in device-quality a-Si,Ge:H alloy material. Second, they reported results of their measurements on a-Si,Ge:H alloy "cathodic" samples produced at Harvard University; these samples were found to exhibit significantly lower defect densities in the high Ge composition range (>50at.% Ge) than alloy samples produced either by conventional glow discharge of photo-chemical vapor deposition. Third, they performed voltage pulse stimulated capacitance transient measurements on a-Si:H/a-Si,Ge:H heterostructure samples to look for carrier trapping states that might be associated with this interface; they found there was a clear signature of trapped hole emission extending over long times associated specifically with the interface itself in concentrations of roughly 10^{11} cm^{-2}. Fourth, researchers reported the results on several hot-wire a-Si:H samples produced with varying hydrogen levels. Their studies indicate that hot-wire-produced a-Si:H, with H levels between 2-5at.%, should lead to mid-gap devices with superior properties. Finally, they discussed some results on glow-discharge material, as well electron-cyclotron-resonance-deposited a-Si:H grown under hydrogen dilution conditions, and confirmed that, in terms of deep-defect creation, such films exhibited improved stability compared to conventional glow-discharge material.

14. SUBJECT TERMS
photovoltaics ; thin films ; amorphous silicon-germanium alloys ; hot-wire deposition ; heterojunction interfaces ; stability ; drive-level capacitance (measurements) ; photocapacitance (measurements)

15. NUMBER OF PAGES
68

16. PRICE CODE

17. SECURITY CLASSIFICATION OF REPORT	18. SECURITY CLASSIFICATION OF THIS PAGE	19. SECURITY CLASSIFICATION OF ABSTRACT	20. LIMITATION OF ABSTRACT
Unclassified	Unclassified	Unclassified	UL